Grain-damage hysteresis and plate tectonic states

David Bercovici[a,*], Yanick Ricard[b]

[a] *Yale University, Department of Geology & Geophysics, New Haven CT, USA*
[b] *Laboratoire de Geólogie de Lyon, ENS-Lyon, Université de Lyon-1, CNRS, Lyon France*

Abstract

Shear localization in the lithosphere is an essential ingredient for understanding how and why plate tectonics is generated from mantle convection on terrestrial planets. The theoretical model for grain-damage and pinning in two-phase polycrystalline rocks provides a frame-work for understanding lithospheric shear weakening and plate-generation, and is consistent with laboratory and field observations of mylonites. Grain size evolves through the competition between coarsening, which drives grain-growth, and damage, which drives grain reduction. The interface between crystalline phases controls Zener pinning, which impedes grain growth. Damage to the interface enhances the Zener pinning effect, which then reduces grain-size, forcing the rheology into the grain-size-dependent diffusion creep regime. This process thus allows damage and rheological weakening to co-exist, providing a necessary positive self-weakening feedback. Moreover, because pinning inhibits grain-growth it promotes shear-zone longevity and plate-boundary inheritance. However, the suppression of interface damage at low interface curvature (wherein inter-grain mixing is inefficient and other energy sinks of deformational work are potentially more facile) causes a hysteresis effect, in which three possible equilibrium grain-sizes for a given stress coexist: (1) a stable, large-grain, weakly-deforming state, (2) a stable, small-grain, rapidly-deforming state analogous to ultramylonites, and (3) an unstable, intermediate grain-size state perhaps comparable to protomylonites. A comparison of the model to field data suggests that shear-localized zones of small-grain mylonites and ultra-mylonites exist at a lower stress than the co-existing large-grain porphyroclasts, rather than, as predicted by paleopiezometers or paleowattmeters, at a much higher stress; this interpretation of field data thus allows localization to relieve instead of accumulate stress. The model also predicts that a lithosphere that deforms at a given stress can acquire two stable deformation regimes indicative of plate-like flows, i.e, it permits the coexistence of both slowly deforming plate interiors, and rapidly deforming plate boundaries. Earth seems to exist squarely inside the hysteresis loop and thus can have coexisting deformation states, while Venus appears to straddle the end of the loop where only the weakly deforming branch exists.

Keywords: Plate generation; mantle convection; damage mechanics

1. Introduction

The existence of plate tectonics is a unique occurrence in our solar system, since Earth is the only known terrestrial planet with a mobile lithosphere that exchanges volatiles and minerals with the surface. Earth's ostensible twin Venus may have sporadic or episodic overturning events as evident in its 500Myr old surface (Turcotte et al., 1999), and Mars might have had plate tectonics very early in its history (Connerney et al., 2005). That planets can transition from stagnant to plate-tectonic states, and/or become fixed in one state or the other, has led to the suggestion that stagnant and mobile states can coexist for given planetary conditions in an effective hysteresis loop; thus a planet's tectonic state may depend not only on its existing conditions, but on its initial conditions and evolutionary path as well. Sleep (2000) originally proposed that stagnant and mobile states of low and high surface heat flow may coexist, and that a planet jumps from one state to the other as internal temperature changes, or the planet might entirely miss the plate-like state when transitioning from the magma-ocean state (see also Sleep, 2015). Likewise Lenardic and Crowley (2012) and Weller and Lenardic (2012) have argued that different tectonic states might be reached during a planet's evolution, even as it converges on the same interior and surface thermal condi-

*Corresponding author
Email addresses: david.bercovici@yale.edu (David Bercovici), yanick.ricard@ens-lyon.fr (Yanick Ricard)

tions; indeed Weller et al. (2015) propose that transitions between these states might be triggered by climatic variations at the surface.

Any prediction about tectonic state, however, depends on what physics governs this state, i.e., what allows mantle convection to become plate-like at the surface. The question of how plates are generated is, in itself, a grand-challenge of geodynamics and a widely studied subject (see reviews by Bercovici, 2003; Bercovici et al., 2015b). In particular, heat-flow and internal temperature are not sufficient causes of a plate-like state and are more likely effects of plate-like convection. Plate-like motion is caused by non-linear rheological behavior, since strong plates are separated by weak plate boundaries nominally at the same temperature, and are thus the result of self-weakening and shear-localization. Simple non-Newtonian rheologies like visco- and pseudo-plastic models, prescribe effective yielding behavior that permits weak and strong zones (i.e., those at or below the yield stress), and such behavior leads to hysteresis depending on how the yield stress is approached (i.e., from high or low stress states, which are inevitably controlled by convective vigor and the thermal evolution of the planet; see Weller and Lenardic, 2012). However, plasticity, like other instantaneous rheologies, disallows any longevity for weak zones, since it predicts they would vanish once they stop deforming. Dormancy and inheritance of weak zones are important components of plate generation since they likely play key roles in subduction zone initiation (Gurnis et al., 2000, 2004; Lebrun et al., 2003) and even the early origin of plate tectonics (Bercovici and Ricard, 2014).

A vital clue about the rheological behavior of plate boundaries and their formation is the pervasiveness of mylonites, which are evidence of severe grain-reduction coincident with extreme deformation in the lithosphere (e.g., White et al., 1980; Jin et al., 1998; Furusho and Kanagawa, 1999; Dijkstra et al., 2004; Warren and Hirth, 2006; Skemer et al., 2010; Tasaka et al., 2014; Linckens et al., 2011, 2015). Mylonites have been the subject of numerous studies and are the primary motivation for models of grain damage and grain-size reduction as a mechanism for lithospheric self-weakening (e.g., Braun et al., 1999; Montési and Hirth, 2003; Landuyt and Bercovici, 2009a; Rozel et al., 2011; Bercovici and Ricard, 2005, 2012, 2013). While shallower lithospheric layers might undergo weakening due to brittle failure and sliding, and hydration-induced weakening in phyllosilicates (e.g., Gueydan et al., 2014), mylonitization likely dominates where the lithosphere is strongest, in the cold ductile regime (around temperatures of 1000K), which imposes the most severe localization bottle-neck. In addition, the slow grain-growth and long healing time-scale, especially when secondary phases are present (Warren and Hirth, 2006; Hiraga et al., 2010; Herwegh et al., 2011; Bercovici and Ricard, 2012), provides memory and inheritance of previous weak zones (Bercovici and Ricard, 2014). Thus, the grain-scale physics occurring in mylonites is likely critical for understanding processes at the global and planetary scale.

Here we expand on the two-phase grain-damage theory of Bercovici and Ricard (2012) by proposing a new but small change to the damage formalism. The basic grain-damage hypothesis states that a small fraction of energy is extracted from deformational work and stored as surface energy on grain boundaries in the process of making smaller grains. Most of the deformational work is still deposited as dissipative heating (assuming long time scales and viscous behavior), but even a small extracted fraction of work is sufficient to drive substantive damage by creation of surface energy. In single phase media, grain-damage and the creation of grain-boundary surface energy only occurs in the dislocation creep regime via dynamic recrystallization (Karato et al., 1980), wherein new grain-boundaries are created by the accumulation of dislocations; in this case, grain reduction does not cause self-weakening since dislocation-creep rheology is grain-size independent. If the grain-size is reduced into the diffusion-creep regime, in which rheology is grain-size dependent, then damage ceases and the grains can only grow (De Bresser et al., 2001; Rozel et al., 2011).

In a two-phase or polycrystalline mixture, such as peridotite (with primarily an olivine-pyroxene mix), surface energy is expressed in two modes, as energy on grain boundaries and on the interface between different mineral components or phases (i.e., the boundary between grains of different composition). In this case, damage and the creation of more surface energy causes both the grain-size and the interface roughness (i.e., radius of curvature) to reduce. We distinguish these processes as *grain-boundary damage* (driven by accumulation of dislocations) and *interface damage* (driven by interface distortion and inter-phase mixing). However the interface roughness and grain evolution also interact through Zener pinning (Smith, 1948; Manohar et al., 1998), wherein the interface blocks grain-boundary migration and hence impedes grain-growth; moreover, the sharper the interface or smaller the pinning bodies, the more effective the blocking or pinning of grain-boundary migration. Therefore, in a two-phase medium, the damage to the interface and reduction of

its roughness (i.e., to make it sharper) results in more effective pinning, which holds down and even reduces the grain-size of both phases, even within the diffusion creep regime, thereby allowing self-weakening. The coupled evolution of grain-size in the two phases as well as that of interface roughness leads to both more effective damage and self-weakening during deformation, and suppressed healing during static conditions because of pinning (Bercovici and Ricard, 2012). These coupled evolution laws are thus significantly different than previous models for single-phase media (Hall and Parmentier, 2003; Montési and Hirth, 2003; Bercovici and Ricard, 2005; Austin and Evans, 2007; Ricard and Bercovici, 2009; Rozel et al., 2011), both because they treat the lithospheric material as a more realistic two-phase mixture like peridotite, but also because damage can persist outside the dislocation creep regime.

However the deposition of energy, and thus damage, to grain boundaries and the interface between phases is not necessarily uniform with grain-size or interface roughness. For example, as stated above, damage directly to grain boundaries (i.e., *grain-boundary damage*) only exists via dynamic recrystallization, which ceases if the grains become smaller than the field-boundary grain-size that delineates the transition from diffusion creep (for small grains) to dislocation creep (for large grains) (De Bresser et al., 2001; Rozel et al., 2011). In this paper, we further consider the consequences of damage to the interface between phases (i.e., *interface damage*) being restricted while the interface is of low roughness, i.e., when the interface area is sparse such as when the components are poorly mixed (e.g., see Linckens et al., 2014). With large grains and unmixed components leading to a sparse interface, the propagation of dislocations and dissipative heating are more facile than creating new interface; in this case interface damage would not be preferred and hence suppressed at larger grain-size and interface roughness. The suppression of interface damage until there is sufficient mixing at small grain-size and roughness leads to a hysteresis effect because damage and grain-reduction occurs either at large grains in the presence of dislocation creep, or small well-mixed grains in the presence of diffusion creep, but is suppressed for intermediate grains (Figure 1). The predicted hysteresis yields the coexistence of three deformation states, i.e. (1) a stable strong *creeping* state, comparable to plate interiors or a stagnant lid, (2) a stable weak *mylonite* state with rapid deformation analogous to plate boundaries, and (3) an *intermediate* unstable, potentially velocity-weakening state that represents the transition between stable states. The hysteresis loop also suggests an effective rheology and a deformation map that predicts separate piezometric and mylonitic trends of grain-size reduction (rather than a single piezometric line whose application and existence outside of the dislocation creep regime is questionable).

Finally, the coexistence of stable strong and weak states suggests that plate tectonics occurs when both states are available, thus permitting strong plates and weak boundaries for the same thermal state and/or state of stress or convective vigor. The coexistence of these states occurs for the full range of model parameters characteristic of Earth-like conditions; Earth is also potentially deep enough inside the hysteresis loop that it has been there for much of its history. Venus, with much hotter surface conditions, straddles the end of the hysteresis loop beyond which only the strong, stagnant-lid state exists; this implies that Venus is never, or rarely, in a condition where the strong and weak states coexist, but is always where the strong state is predominantly stable, thus predicting it has either a permanent stagnant lid, or short bursts of plate-like states punctuated by long periods of lithospheric stagnation.

In the following we explain the physical underpinning of energy partitioning that leads to hysteresis, and from there explore the theoretical predictions for the existence of the hysteresis loop, its implications for shear-localization, rheology and interpretation of field observations, and finally planetary tectonics and evolution.

2. Theory and Analysis

2.1. Grain damage, pinning and energy partitioning

In the two-phase grain-damage theory of Bercovici and Ricard (2012), a small fraction of deformational work goes toward creating surface energy in a mixture of grained materials, while the remaining portion of deformational work goes toward dissipative heating (since the continuum is considered viscous). The fraction of work going toward surface energy is itself partitioned between surface energy on grain-boundaries, and the energy on the interface between different phases or components of the mixture (or equivalently the boundary between grains of different composition like olivine and pyroxene in a peridotite mixture). The grain-boundary energy is increased by reducing grain-size, typically by the accumulation and linking of dislocations to make new grain-boundaries; as noted above, we refer to this process as *grain-boundary damage*. Interfacial energy is increased by interface distortion and rending as well inter-phase mixing, and this is referred to as *interface damage*. Such interface damage and sharpening leads to smaller dispersed Zener pinning bodies

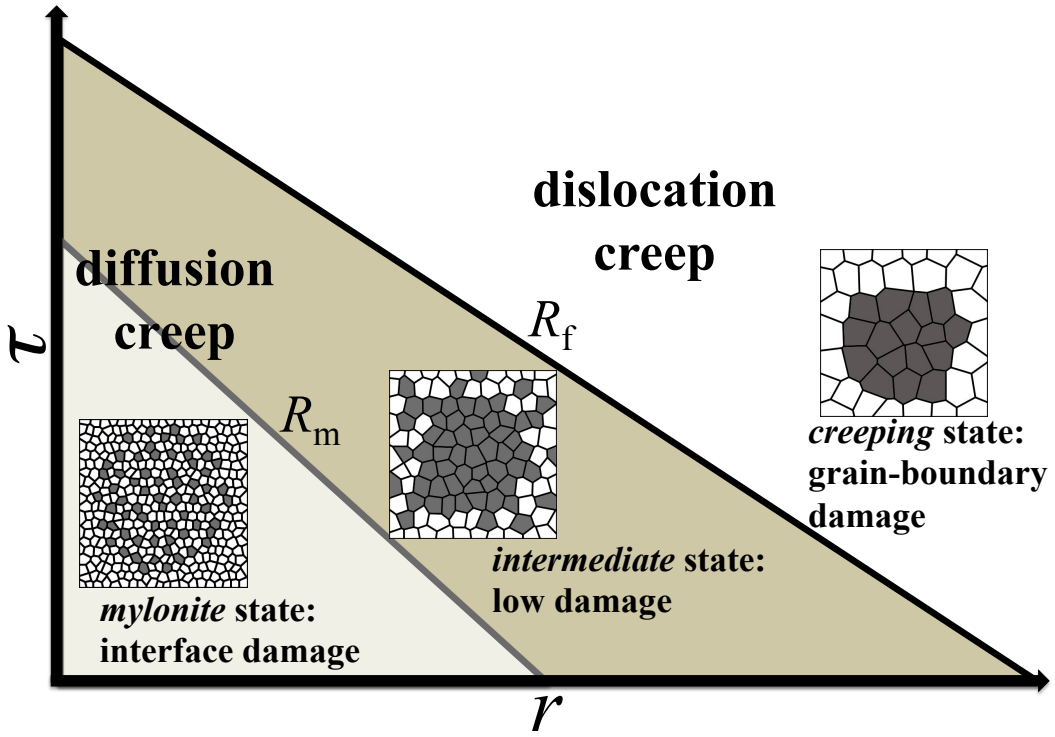

Figure 1: A schematic deformation map, showing transitions in damage and rheological behavior with changing stress τ and interface roughness r, which is also proportional to average grain-size. The medium is assumed to be a two-phase grained material (e.g., a peridotite mixture of olivine and pyroxene) wherein grain-size and interface roughness can evolve. The *creeping* regime is associated with large grains and sparse interface (indicated by the inset) dominated by dislocation creep and grain-boundary damage (i.e., dynamic recrystallization). The *mylonite* regime is associated with a well-mixed medium of small grains and a dense interface (see inset), undergoing diffusion creep and where the interface between phases is damaged by inter-grain mixing and interface distortion and rending. The *intermediate* regime is associated with grains that are small enough to be in diffusion creep (thus grain-boundary damage by dislocations is suppressed), but are not well mixed or dispersed enough for the interface to be damaged; and thus damage in this regime is inefficient. See text for further details.

that, in turn, pin or drive grains to smaller sizes. The total transfer of work energy to surface energy on the grain-boundaries and the interface between phases is the essential *two-phase grain damage* process.

Here we present a simplified version of the two-phase grain-damage model to illustrate the basic physics behind a new hysteresis effect; the development of the adjusted full two-phase grain-damage model is described in Appendix A. In general, the grain-damage model is isotropic and the grain-size in each phase and the interface roughness are represented by single mean sizes. For the simplified model, however, we assume the system is in a *pinned state*, in which the grain-size evolution is entirely dictated by the Zener pinning effect, and hence is slaved to the evolution of the interface radius of curvature or *roughness* r, which itself represents the size of the Zener pinning bodies (see Bercovici and Ricard, 2012, Figure 2). In this pinned state, the grain-sizes of each phase are simply proportional to r, and the average grain-size of the mixture is approximately $\frac{\pi}{2}r$ (see Appendix A.2). (To verify that the pinned-state assumption is not egregious, we consider the full set of governing equations for the coupled evolution of both grain-size and interface curvature, which demonstrates that the hysteretic behavior discussed herein is qualitatively the same, though a bit more complex; see Appendix A.1.) With this assumption, only the evolution of the interface need be considered, as given by (Bercovici and Ricard, 2012, 2013, 2014; Bercovici et al., 2015a)

$$\frac{\mathrm{d}r}{\mathrm{d}t} = \frac{\eta G}{q r^{q-1}} - \frac{r^2}{\eta\gamma} f_\mathrm{I} \overline{\Psi} \tag{1}$$

where t is time, G is the coarsening coefficient for the interface, q is a constant exponent (typically $q = 4$), η is a dimensionless quantity of order unity that controls how the volume fractions of mixture components or phases influence the interface area density, γ is the interface surface tension (i.e., the surface tension between grains of different phases), $\overline{\Psi}$ is the net rate of deformational work; finally f_I is the partitioning fraction of

deformational work going to create surface energy on the interface, i.e., the *interface damage* fraction, where typically $f_\mathrm{I} \ll 1$ since most deformational work goes toward viscous dissipation (see Appendix A for more details).

In previous studies (Bercovici and Ricard, 2012, 2013, 2014; Bercovici et al., 2015a), f_I was assumed a constant. However, here we consider that the partitioning of work toward interface surface energy may be restricted while the interface is smooth and its density (i.e., interface area per unit volume of the mixture) is sparse. In particular if the interface coarsens and the interface area decreases (i.e., r grows), damage to the interface should diminish, especially as other sinks of work energy, such as grain-boundary damage via increased dislocations and dynamic recrystallization, or modes of dissipative heating, are more facile and/or more readily available; in these limits f_I should become very small. But as the interface becomes more distorted toward finer scale (i.e., r reduces), and grain-boundary damage by dislocations becomes unavailable in the diffusion creep regime, then $f_\mathrm{I} \to f$ where f is a maximum partitioning fraction. We prescribe a simple form

$$f_\mathrm{I} = f\frac{R_\mathrm{m}^b + \chi r^b}{R_\mathrm{m}^b + r^b} \tag{2}$$

where $b > 0$ and is a constant, and $\chi < 1$ such that χf is the much reduced asymptotic value of f_I at large r. For simplicity, we later assume in the main analysis of the model that $\chi \approx 0$, but we provide some discussion for cases in which $\chi > 0$ in Appendix A.3.

The quantity R_m represents the roughness (or effective grain-size) r above which interface damage is suppressed. As stated above, interface damage is assumed suppressed in dislocation creep, for large grains and sparse interface (i.e., large r) because grain-boundary damage is dominant. This effect occurs for r greater than the field-boundary roughness R_f, which delineates the transition from dislocation to diffusion creep (see below §2.2 and (5) for mathematical definitions of R_f as well as R_m, both of which are functions of stress; also note that the field-boundary grain-size differs slightly from R_f by a factor of approximately $\pi/2$; see Appendix A.2). Deformation in dislocation creep can still induce weak interface damage, as the sparse or smooth interface is stretched and distorted (which corresponds to a small value of χ).

For $r < R_\mathrm{f}$ dislocation-induced grain-boundary damage becomes suppressed, although this does not mean that interface damage then becomes dominant at $r = R_\mathrm{f}$. In particular, strong interface damage ensues when *both* (a) it is no longer competing with grain-boundary damage in the dislocation creep regime and (b) the grains are small enough to allow efficient inter-grain mixing by grain switching events (e.g., see Linckens et al., 2014). Interface damage thus becomes dominant when the grains are small enough to both be within the diffusion creep regime and to allow effective grain mixing and dispersal. Therefore, the efficiency of interface damage increases as r shrinks below $r = R_\mathrm{f}$ and through a mixing transition, after which f_I saturates at its maximum value of f when the grains are well mixed and dispersed. In this case, R_m represents a transition to a well mixed state in which $R_\mathrm{m} < R_\mathrm{f}$ (Figure 1). This dispersal and stirring of smaller grains of one phase in the other phase enhances the effect of Zener pinning and the influence of interface roughness on grain-evolution (see, e.g., Warren and Hirth, 2006), in particular driving further grain-reduction and self weakening of the system, since it obeys diffusion creep.

Grain mixing, however, is also concomitant with grain-boundary sliding or GBS (Chen and Argon, 1979), which is required for grain switching (e.g., Dimanov et al., 2007; Linckens et al., 2014). Grain-boundary sliding is likely significant even for moderate sized grains in a region of grain-size space straddling the field boundary R_f (possibly even causing a dislocation-accommodated GBS rheology, or "disGBS", although we do not employ this rheology here ; see Hirth and Kohlstedt, 2003; Hansen et al., 2011), and extending down to about 1-10% of R_f (Hansen et al., 2011). We assume below this grain-boundary sliding regime, the system becomes well mixed, and thus R_m is about 1-10% of R_f. For $r < R_\mathrm{m}$ the medium is well dispersed and further mixing and sliding is readily accommodated by the small grain-sizes and facile deformation in diffusion creep. (See summary schematic, Figure 1).

2.2. *Governing equations*

Since the pinned-state assumption averages together the properties of the individual phases and their grains, we assume the stress tensor $\underline{\boldsymbol{\tau}}$ and strain-rate tensor $\underline{\dot{\mathbf{e}}}$ are the same across the phases within an infinitesimal control volume; in this case our composite rheology of dislocation and diffusion creep is (Rozel et al., 2011; Bercovici and Ricard, 2012; Bercovici et al., 2015a)

$$\underline{\dot{\mathbf{e}}} = (A\tau^{n-1} + B/r^m)\underline{\boldsymbol{\tau}} \tag{3}$$

where A and B are dislocation and diffusion creep compliances, respectively, assumed to be the same for both phases; n is the dislocation-creep power-law exponent, m is the diffusion-creep grain-size exponent, and we assume $n = m = 3$ for typical dislocation and Coble creep

laws; lastly, $\tau^2 = \frac{1}{2}\underline{\boldsymbol{\tau}} : \underline{\boldsymbol{\tau}}$ is the 2nd stress invariant. Since the rate of deformational work is $\overline{\Psi} = \underline{\boldsymbol{\tau}} : \underline{\dot{\mathbf{e}}}$, the interface damage equation (1), along with (2) (assuming $\chi = 0$) and (3) becomes

$$\frac{\mathrm{d}r}{\mathrm{d}t} = \frac{\eta G}{q r^{q-1}} - \frac{2 f r^2 (A\tau^{n+1} + B\tau^2/r^m)}{\gamma\eta(1 + (r/R_\mathrm{m})^b)} \tag{4}$$

The field boundary roughness R_f occurs where the strain-rates associated with diffusion and dislocation creep are equal, and we assume the mixing-transition roughness R_m is also a function of stress; ergo

$$R_\mathrm{f} = \left(\frac{B}{A\tau^{n-1}}\right)^{1/m} \quad \text{and} \quad R_\mathrm{m} = \left(\frac{\mathcal{K}}{\tau}\right)^{\alpha/b} \tag{5}$$

where $\mathcal{K}$ is a proportionality factor and α is a constant If R_m follows the lower grain-boundary sliding transition (as discussed in §2.1), then $R_\mathrm{m} < R_\mathrm{f}$; moreover if this transition is nearly parallel to the field-boundary in $r - \tau$ space (see Hansen et al., 2011) it suggests that $\alpha = b(n-1)/m$. Even if R_m and R_f are not parallel, we generally assume that $R_\mathrm{m} < R_\mathrm{f}$ in the range of stresses that we consider; i.e. the two boundaries only intersect at stresses that are unrealistically high, or so low that no deformation occurs anyway.

2.3. Dimensionless governing equations

Analysis of the system's hysteretic behavior only requires the rheological and interface damage equations, (3) and (4), respectively, along with the definitions in (5). Given a characteristic reference or driving stress scale $\boldsymbol{\tau}_\circ$, then the strain-rate (or inverse time) and roughness scales are

$$\dot{\mathsf{E}} = A\boldsymbol{\tau}_\circ^n \quad \text{and} \quad \mathsf{R} = \left(\frac{B}{A\boldsymbol{\tau}_\circ^{n-1}}\right)^{1/m}, \tag{6}$$

which are, respectively, the dislocation creep strain-rate scale, and the roughness on the field boundary associated with $\boldsymbol{\tau}_\circ$. Thus, nondimensionalizing $\underline{\boldsymbol{\tau}}$ by $\boldsymbol{\tau}_\circ$, $\underline{\dot{\mathbf{e}}}$ and $1/t$ by $\dot{\mathsf{E}}$, and r, R_f and R_m by R, the dimensionless governing equations for rheology and damage become

$$\underline{\dot{\mathbf{e}}} = (\tau^{n-1} + 1/r^m)\underline{\boldsymbol{\tau}} \tag{7}$$

and

$$\frac{\mathrm{d}r}{\mathrm{d}t} = \frac{C}{q r^{q-1}} - \mathcal{D}\frac{r^2\left(\tau^{n+1} + \tau^2/r^m\right)}{1 + (r/\mathsf{R}_\mathrm{m})^b \tau^\alpha} \tag{8}$$

where

$$C = \frac{\eta G}{\mathsf{R}^q A \boldsymbol{\tau}_\circ^n} \quad \text{and} \quad \mathcal{D} = \frac{2 f \mathsf{R} \boldsymbol{\tau}_\circ}{\gamma_1 \eta} \tag{9}$$

are the coarsening (or healing) and damage numbers, respectively, As discussed previously (Bercovici and Ricard, 2013, 2014; Bercovici et al., 2015a) typical Earth-like values are $C \approx 10^{-5}$ and $1 \le \mathcal{D} \le 1000$, which are based on dry olivine laboratory data for rheologies (Hirth and Kohlstedt, 2003), damage partitioning fraction f (Austin and Evans, 2007; Rozel et al., 2011) and grain and interface coarsening laws (Karato, 1989; Bercovici and Ricard, 2012) at a mid-lithosphere temperature around 1000K. Moreover, $\mathsf{R}_\mathrm{m} = (\mathcal{K}/\boldsymbol{\tau}_\circ)^{\alpha/b}\mathsf{R}^{-1}$, and since we assume R_m falls below the field boundary then $\mathsf{R}_\mathrm{m} < 1$, and in particular, given the arguments at the end of §2.1, we assume $10^{-2} \le \mathsf{R}_\mathrm{m} \le 10^{-1}$. Therefore, the dimensionless field boundary and mixing-transition roughness are

$$R_\mathrm{f} = \tau^{(1-n)/m} \quad \text{and} \quad R_\mathrm{m} = \mathsf{R}_\mathrm{m}\tau^{-\alpha/b} \tag{10}$$

A summary of dimensionless variables and parameters is given in Table 1.

2.4. Preliminary Analysis

The model hysteretic behavior and its implications for lithosphere rheology, localization and planetary evolution can be gained from basic analysis of the model equations. In particular, analyses of the equilibrium states and their stability will be common to all the applications of interest.

2.4.1. Equilibrium

The damage equation (8) in the steady-state limit gives

$$0 = \frac{C}{q r^{q-1}} - \mathcal{D} r^2 \tau^{n+1} \frac{1 + (R_\mathrm{f}/r)^m}{1 + (r/R_\mathrm{m})^b} \tag{11}$$

where R_f and R_m are defined in (10). Although this equation can be solved numerically for arbitrary parameters (see §3.2), we infer three approximate solutions to (11) for r outside and inside the field and mixing boundaries, i.e., (a) $r \gg R_\mathrm{f} > R_\mathrm{m}$, (b) $r \ll R_\mathrm{m} < R_\mathrm{f}$, and (c) $R_\mathrm{m} < r < R_\mathrm{f}$ in which there is a domain (given that typically $m \ge 2$ and we later show $b > 2$) that $(R_\mathrm{f}/r)^m \gg 1$ and $(r/R_\mathrm{m})^b \gg 1$. These limits yield, using the definition of R_f and R_m in (10), the approximate solutions

$$\tau^{n+1-\alpha} = \frac{C}{q\mathcal{D}\mathsf{R}_\mathrm{m}^b} r^{b-q-1} \qquad \text{for } r \gg R_\mathrm{f} \tag{12a}$$

$$\tau^{2-\alpha} = \frac{C}{q\mathcal{D}\mathsf{R}_\mathrm{m}^b} r^{b+m-q-1} \qquad \text{for } R_\mathrm{m} < r < R_\mathrm{f} \tag{12b}$$

$$\tau^2 = \frac{C}{q\mathcal{D}} r^{m-q-1} \qquad \text{for } r \ll R_\mathrm{m} \tag{12c}$$

Table 1: Table of dimensionless model variables and parameters.

Variable	Definition	Reference Equation(s)
r	interface roughness	(8)
$\underline{\boldsymbol{\tau}}$	stress tensor	(7)
τ	square-root of 2nd stress invariant	$\tau^2 = \frac{1}{2}\underline{\boldsymbol{\tau}} : \underline{\boldsymbol{\tau}}$
$\underline{\dot{\boldsymbol{\varepsilon}}}$	strain-rate tensor	(7)
$\dot{e}$	square-root of 2nd strain-rate invariant	$\dot{e}^2 = \frac{1}{2}\underline{\dot{\boldsymbol{\varepsilon}}} : \underline{\dot{\boldsymbol{\varepsilon}}}$
R_f	dislocation-diffusion creep field boundary roughness	(10)
R_m	mixing transition roughness	(10)
u	shear velocity	(17)

Parameter	Definition	Reference Equation and typical values
C	interface coarsening rate	(9), $10^{-5} \leq C \leq 10^{-2}$
$\mathcal{D}$	interface damage rate	(9) $1 \leq \mathcal{D} \leq 1000$
n	dislocation creep stress exponent	(7), $n = 3$
m	diffusion creep grain-size exponent	(7), $m = 3$
q	interface coarsening exponent	(8), $q = 4$
R_m	reference mixing transition roughness	(10), $10^{-2} \leq \mathsf{R}_\mathrm{m} \leq 10^{-1}$
b	interface damage saturation roughness exponent	(2), $b = 4$
α	interface damage saturation stress exponent	(10), $0 \leq \alpha \leq 8/3$

We refer to these three branches as the *creeping*, *intermediate* and *mylonite* states, respectively. The *creeping* branch (12a) occurs at large grain-sizes in the dislocation creep regime and (as discussed below) can be associated with the paleowattmeter relation (Austin and Evans, 2007). The *mylonite* branch (12c) represents an independent trend for small grains being influenced by interface damage in diffusion creep. The *intermediate* branch (12b) is the transition between the other branches, and as shown below is unstable and can be associated with velocity weakening for certain parameter choices. The full solution to (11), or the approximations given by (12), also comprise theoretical states on a deformation map, as discussed in §3.2 and summarized in Table 2.

The intersections of the branches described in (12) delineate the transition from *creeping* to *intermediate* to *mylonite* states (as well as stress extrema, as shown below in §3.2). These intersections occur, unsurprisingly, at $r = R_\mathrm{f}$ and $r = R_\mathrm{m}$, for the *creeping–intermediate* and *mylonite–intermediate* transitions, respectively; this result arises simply from dividing either (12a) or (12c) by (12b).

2.4.2. Stability

The stability of the equilibrium states can be determined by looking at the growth rate of a perturbation to the steady state at a given stress τ, such that $r = r_0 + \epsilon e^{st}$ where $\epsilon \ll 1$; when substituting this expansion into (8) and linearizing it to $O(\epsilon^1)$, the resulting growth rate is

$$s = -\frac{C}{q r_0^q}\left(q + 1 - \frac{m}{1 + (r_0/R_\mathrm{f})^m} - \frac{b(r_0/R_\mathrm{m})^b}{1 + (r_0/R_\mathrm{m})^b}\right) \quad (13)$$

where r_0 is the solution to (11) and R_f and R_m are given by (10). For the same limits delineated in (12), we find that $s' \approx -(q + 1 - b)$ for the *creeping* branch (i.e. $r_0 \gg R_\mathrm{f}$), $s' \approx -(q + 1 - m)$ for the *mylonite* branch ($r_0 \ll R_\mathrm{m}$), and $s' \approx -(q + 1 - m - b)$ for the *intermediate* branch ($R_\mathrm{m} < r_0 < R_\mathrm{f}$), respectively, where $s' = s \cdot q r_0^q / C$. For the junction of the *creeping* and *intermediate* branches, at the field boundary where $r = R_\mathrm{f} \gg R_\mathrm{m}$, $s' \approx -(q + 1 - m/2 - b)$, while for the junction of the *mylonite* and *intermediate* branches, where $r = R_\mathrm{m} \ll R_\mathrm{f}$, $s' \approx -(q + 1 - m - b/2)$. For typical values of $q = b = 4$ and $m = 3$ (see §2.4.4) the *creeping* and *mylonite* branches are generally stable ($s < 0$), while the *intermediate* branch is generally unstable ($s > 0$); one exception occurs for the junction at the field boundary $r = R_\mathrm{f}$, where the *creeping* branch is also unstable ($s' = 1/2$), while for the other junction at $r = R_\mathrm{m}$, the *mylonite* and *intermediate* branches are marginally stable ($s' = 0$).

2.4.3. An interlude with some physical interpretation

Given the three equilibrium branches and their stability, we can gain some physical intuition about the possible states of our model system. None of the equilibria are static since they represent the continuous balance

between grain and interface coarsening and comminution by damage, when averaged over a small control volume. The *creeping* branch represents a stable state wherein interface damage occurring in the dislocation-creep regime is weakened by a diminished work partitioning fraction $f_1(r)$, and is balanced by weak healing that occurs for a coarse interface; dynamic recrystallization and grain-growth are also implicitly in balance along this branch, although they are weakened because of the proximity to the field boundary R_f (see Appendix A and in particular (A.5)) and by pinning, respectively. The *mylonite* branch represents a likewise stable state, but wherein strong damage in diffusion creep, with a maximal $f_1(r)$, is balanced by strong healing at very small roughness r and grain-sizes. The *intermediate* branch represents the balance of moderately weakened damage against modest healing for small grains between the boundaries $r = R_f(\tau)$ and $r = R_m(\tau)$; this branch is unstable because if pinning bodies and grains in this state become slightly smaller they approach stronger damage conditions, which drive grains smaller yet, and if they become slightly larger they approach weaker damage conditions allowing healing to dominate and drive further grain growth.

Finally, for the sake of comparison, we note the behavior of the solution branches when f_1 is constant, as assumed in our previous studies. For this case, we take the limit of $\mathsf{R}_m \to \infty$, which yields only the *creeping* and *mylonite* branches (equivalent to (12a) and either (12b) or (12c) with $\alpha = b = 0$) that are connected at the field boundary $r = R_f$. In this case the solution branch is a monotonic and continuous function $\tau(r)$ (with a slope change at $r = R_f$) and thus disallows hysteresis and the coexistence of multiple deformation states.

2.4.4. *Some parameter constraints*

As previously inferred (Bercovici and Ricard, 2012, 2013, 2014; Bercovici et al., 2015a) we use $q = 4$ for the roughness healing exponent, and $m = n = 3$ for standard dislocation and Coble diffusion creep laws. The parameters b and α are unique to the new features of our model, and here we estimate some constraints on their values.

First, we consider that the *creeping* branch, which occurs at large grain-sizes in the dislocation creep regime, can be associated with the relations for a paleopiezometer (e.g., Van der Wal et al., 1993; Stipp et al., 2010) or more appropriately a paleowattmeter (Austin and Evans, 2007), which is based on the same grain-damage principles stated in Bercovici and Ricard (2005) and Rozel et al. (2011). The paleowattmeter relation suggests that $\tau^{n+1} \sim 1/r^{p+1}$ where p represents the single-phase (e.g., olivine) grain-growth exponent, similar to q (see also Appendix A); equating this relation to (12a) suggests that $\alpha = (n+1)(p+b-q)/(p+1)$.

A second possible constraint arises by assuming that R_m is parallel to R_f in $r - \tau$ space (see §2.2) such that $\alpha = b(n-1)/m$. Combining this with the paleowattmeter constraint uniquely determines α and b. For example, the olivine piezometer and paleowattmeter suggests $p = 2$ (Austin and Evans, 2007), and using $m = n = 3$ and $q = 4$ leads to $b = 4$ and $\alpha = 8/3$.

Even the best constraints considered so far only provide some guidance or suggestions for values of b and α. For example, there is no strict requirement that R_m be parallel to R_f except that it guarantees that $R_m < R_f$ under any conditions. Likewise, the paleowattmeter for pure olivine (i.e., $p = 2$) may not apply to our polycrystalline (two-phase) model of a peridotite. However, to limit the size of parameter space, throughout the rest of the paper we will assume $b = 4$ and explore the system behavior for a range of α, including $\alpha = 8/3$ as well as some other important values. Finally, the *creeping* branch (see (12a)) only has the correct trend of τ decreasing with r if $\alpha < n + 1 = 4$, and thus we limit its range to $0 \le \alpha < 4$.

3. Results

3.1. *Hysteresis branches and their stability*

A basic feature of hysteresis and shear-localization is that a given stress potentially produces at least two possible deformation states, in particular low strain rate and high strain rate (or equivalently large grain-size and small grain-size) states, characteristic of, for example, strong slowly deforming tectonic plate interiors and weak, rapidly deforming plate boundaries. This effect is mostly easily demonstrated by considering the system for one given dimensional stress $\boldsymbol{\tau}_\circ$ by which we nondimensionalize our equations, such that the dimensionless stress is $\tau = 1$. In this case, (11) becomes a polynomial in r, with the three approximate solutions given by (12) with $\tau = 1$. The full solution to (11) with $\tau = 1$ displays the hysteresis curve with three states or branches, i.e., the large-grain *creeping* state, the small-grain *mylonite* state, and the *intermediate* connecting branch (Figure 2a); these full solutions also verify the approximate solutions (12) with $\tau = 1$

The behavior of the hysteresis loop is evident by considering that as the damage-to-healing ratio $q\mathcal{D}/C$ increases from zero, first only the large roughness and grain equilibrium state is available on the *creeping* branch, but with increasing $q\mathcal{D}/C$ that branch

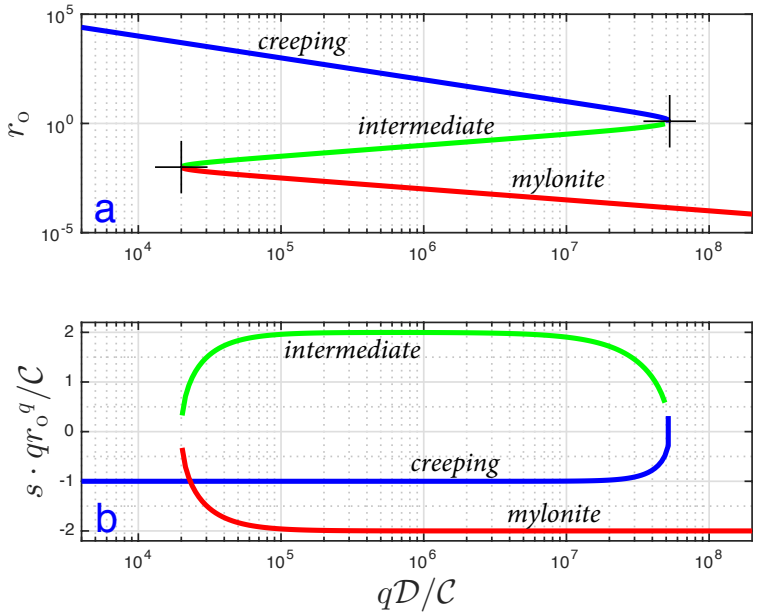

Figure 2: Equilibrium states (a) and their growth rates and stability (b) as described in §3.1. The *creeping* *intermediate* and *mylonite* branches are both labeled accordingly and indicated by blue, green and red, respectively. Calculations are for $q = b = 4$, $m = n = 3$ and $\mathsf{R}_\mathrm{m} = 10^{-2}$. The intersection of the approximate branch solutions (12) for $\tau = 1$ are at $r = R_\mathrm{f} = 1$ and $r = R_\mathrm{m} = \mathsf{R}_\mathrm{m}$, respectively, and are indicated by black crosses.

eventually truncates and the system must jump to the small grain *mylonite* branch. If the trend in the damage:healing ratio is reversed, the *mylonite* branch persists but also eventually truncates and the system jumps back to the *creeping* branch, but at a very low value of $q\mathcal{D}/C$. Within the hysteresis loop, the three branches or states co-exist, however the *intermediate* branch is not necessarily attainable through the hysteresis cycle if the system adheres close to equilibrium.

The intersection of the *creeping* and *mylonite* branches with the *intermediate* branch occur at $r = R_\mathrm{m} = \mathsf{R}_\mathrm{m}$ and $r = R_\mathrm{f} = 1$, respectively. The damage to healing ratio at which these intersections occur are $q\mathcal{D}/C = \mathsf{R}_\mathrm{m}^{-b}$ and $\mathsf{R}_\mathrm{m}^{-(q+1-m)}$ for the *creeping* and *mylonite* branches, respectively. Therefore, since $\mathsf{R}_\mathrm{m} < 1$ the hysteresis loop only exists (i.e., the three branches coexist within a finite range of $q\mathcal{D}/C$) for $b > q + 1 - m$, or specifically $b > 2$ for $q = 4$, $m = 3$, which is satisfied by our choice of $b = 4$.

The stability of the hysteresis branches can also be determined from (13) for $\tau = 1$, which shows (Figure 2b) that the *mylonite* and *creeping* (i.e., small and large grain) branches are stable ($s < 0$), except very near the transition from *creeping* to *intermediate* branches, at $r = R_\mathrm{f}$, while the *intermediate* branch is unstable ($s > 0$), and thus cannot be maintained even if it could be reached. However, the intermediate branch is important for ascertaining which stable branch the system evolves toward depending on what side of the equilibrium *intermediate* branch it begins (Figure 2a); in effect the unstable *intermediate* branch represents a ridge and the stable branches are valleys.

3.2. *Effective Rheology*

An effective rheology for the hysteresis model can be estimated from the equilibrium state solution to (11); this gives a relation for $r(\tau)$ (e.g., (12)), which can then be substituted into the 1-D (or 2nd invariant) version of the composite rheology law (7) to yield an effective constitutive law $\dot{e}(\tau)$ (Figure 3). This constitutive relation allows the coexistence of three strain-rates for a given stress, i.e, a low-strain high-viscosity state associated with the *creeping* branch, a low-viscosity high-strain-rate state for the *mylonite* branch, and an intermediate and potentially velocity weakening state for the unstable *intermediate* branch. This constitutive law is characteristic of shear-localizing behavior in that it allows coexistence of both low and high strain-rate states for a given stress. Although velocity weakening behavior itself is often identified with shear-localization, it is also intrinsically unstable in that it promotes run-away weakening to infinite strain-rate. While our model can feature an unstable velocity-weakening *intermediate* branch, the highest and lowest strain-rate states, i.e., the *creeping* and *mylonite* branches, are stable (Figure 3).

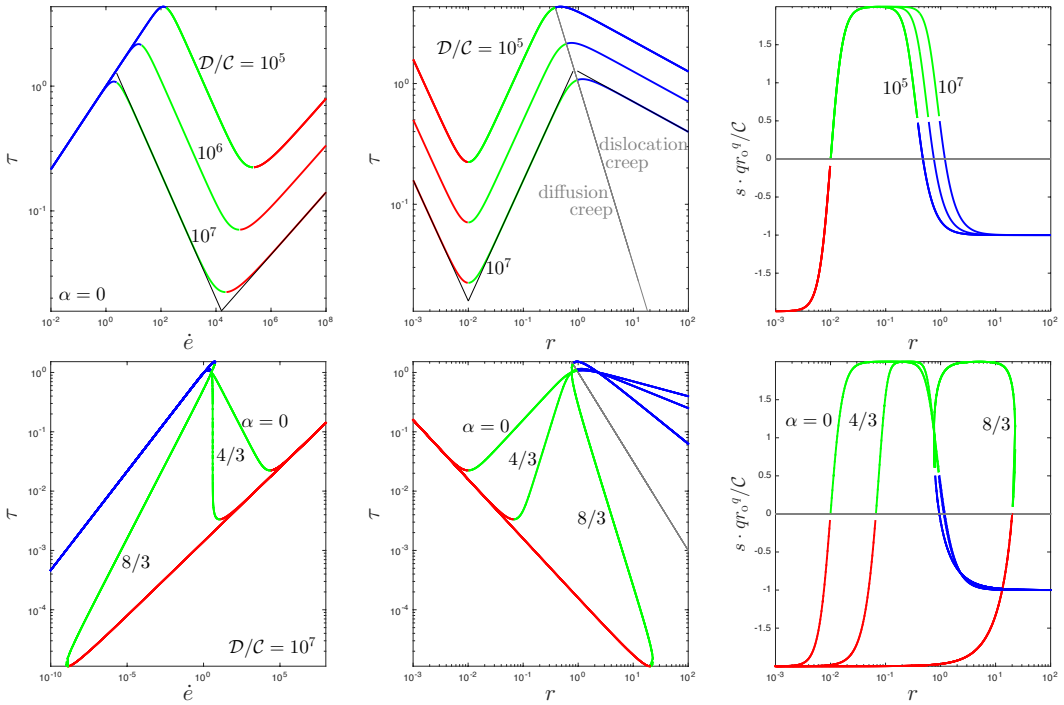

Figure 3: Effective constitutive law $\tau(\dot{e})$ (left column), deformation map $\tau(r)$ (middle column) and stability of each branch $s(r)$ (right column) for three different $\mathcal{D}/\mathcal{C}$ for a fixed α (top row) and three α for fixed $\mathcal{D}/\mathcal{C}$ (bottom row). The thin black lines parallel to some of the solutions are examples of the asymptotic solutions given by (12) and (14). The field boundary $\tau^{n-1} = r^m$ is indicated by the thin gray line on the deformation maps. For all cases $q = b = 4$, $n = m = 3$ and $\mathsf{R}_\mathrm{m} = 10^{-2}$, and the association of line colors with the three branch solutions are the same as in Figure 2.

Approximate constitutive relations for three rheological branches can be gleaned by considering the approximate solutions for $r(\tau)$ given by (12), and substituting them into the 1-D version of (7). However, to be consistent with the *creeping* branch assumption of $r \gg R_\mathrm{f}$ we use the dislocation-creep limit, which does not require knowledge of r, while for the other two branches, we have assumed $r < R_\mathrm{f}$ and thus the rheology is dominated by diffusion creep. For these limits we arrive at

$$\dot{e} = \tau^n \qquad \text{for } r \gg R_\mathrm{f} \qquad (14a)$$

$$\dot{e} = \left(\frac{q\mathcal{D}\mathsf{R}_\mathrm{m}^b}{\mathcal{C}}\right)^{\frac{m}{q+1-m-b}} \tau^{\frac{q+1+m-b-m\alpha}{q+1-m-b}} \qquad \text{for } R_\mathrm{m} < r < R_\mathrm{f} \qquad (14b)$$

$$\dot{e} = \left(\frac{q\mathcal{D}}{\mathcal{C}}\right)^{\frac{m}{q+1-m}} \tau^{\frac{q+1+m}{q+1-m}} \qquad \text{for } r \ll R_\mathrm{m} \qquad (14c)$$

for the *creeping* , *intermediate* and *mylonite* branches respectively. Direct solutions to the equilibrium equation (11) also give deformation map relations $\tau(r)$, as approximated by (12) (Figure 3). The stability of the three branches in the deformation-map can also be discerned from (13), and verifies that the *intermediate* branch is unstable regardless of whether it is velocity weakening or not, that the *mylonite* branch is always stable, and the *creeping* branch is stable except near the field boundary $r = R_\mathrm{f}$ (see Fig. 3 and §2.4.2).

The constitutive laws and deformation map relations for the three branches are summarized, using the fixed parameter values $q = b = 4$, $n = m = 3$, in Table 2. As noted in §2.4.4, the *creeping* deformation-map curve only has the correct trend for $\alpha < 4$, and matches an olivine paleowattmeter (Austin and Evans, 2007) for $\alpha = 8/3$. The *mylonite* branch is independent of the choice of α, and obeys an effective power-law rheology that is a bit more nonlinear than dislocation creep. The *intermediate* branch follows a velocity-weakening rheology if $\alpha < 4/3$; at $\alpha = 4/3$ the constitutive law makes an effectively discontinuous transition from the *creeping* to *mylonite* branches, and follows a constant strain-rate curve $\tau \sim r^m = r^3$ on the deformation map (Figure 3).

Since stress τ is multivalued for both strain-rate $\dot{e}$ and r, hysteretic behavior always exists for cycling up and down in stress provided $b > q + 1 - m = 2$ (as discussed

Table 2: Summary of rheological relations for different hysteresis branches*

quantity ref. eqn.	*mylonite* stable	*intermediate* unstable	*creeping* stable (mostly)
τ deform. map (12)	$\left(\frac{C}{4\mathcal{D}}\right)^{\frac{1}{2}} r^{-1}$	$\left(\frac{C}{4\mathcal{D}\mathsf{R}_\mathrm{m}^4}\right)^{\frac{1}{2-\alpha}} r^{\frac{2}{2-\alpha}}$	$\left(\frac{C}{4\mathcal{D}\mathsf{R}_\mathrm{m}^4}\right)^{\frac{1}{4-\alpha}} r^{-\frac{1}{4-\alpha}}$
$\dot{e}$ constit. law (14)	$\left(\frac{4\mathcal{D}}{C}\right)^{\frac{3}{2}} \tau^4$	$\left(\frac{4\mathcal{D}\mathsf{R}_\mathrm{m}^4}{C}\right)^{-\frac{3}{2}} \tau^{\frac{3\alpha-4}{2}}$	τ^3
$\tau_{\mathrm{min,max}}$	$\left(\frac{2\mathcal{D}\mathsf{R}_\mathrm{m}^2}{C}\right)^{-\frac{2}{4-\alpha}}$	$\left(\frac{8\mathcal{D}\mathsf{R}_\mathrm{m}^4}{C}\right)^{-\frac{3}{10-3\alpha}}$	

∗ Using $q = b = 4$ and $n = m = 3$

in §2.4.4); i.e., the jumps between *creeping* and *mylonite* branches occur at different $\dot{e}$ and r depending on whether stress is increasing or decreasing. However, the hysteresis loop for cycling in $\dot{e}$ exists at different values of α. In particular, for $\alpha < 4/3$, the transition between *creeping* and *mylonite* branches for cycling in $\dot{e}$ occurs smoothly and reversibly along a velocity weakening *intermediate* branch, and is thus non-hysteretic. However, the constitutive law involves a hysteresis loop in strain-rate for $\alpha > 4/3$, since cycling in strain-rate involves jumps between the *creeping* and *mylonite* branches at different stresses and strain-rates.

The maximum and minimum stresses are approximately given by the intersection of the deformation map curve (11) with the boundaries $r = R_\mathrm{f} = \tau^{(1-n)/m}$ and $r = R_\mathrm{m} = \mathsf{R}_\mathrm{m}\tau^{-\alpha/b}$, respectively (and also approximated, more crudely, by the intersection of the *creeping* and *mylonite* lines with the *intermediate* line, given by (12)); these intersections lead to

$$\tau_{\max} = \left(\frac{2q\mathcal{D}\mathsf{R}_\mathrm{m}^b}{C}\right)^{\frac{m}{(n-1)(q+1-b)-m(n+1-\alpha)}}$$
$$\tau_{\min} = \left(\frac{q\mathcal{D}\mathsf{R}_\mathrm{m}^{q+1-m}}{2C}\right)^{\frac{b}{\alpha(q+1-m)-2b}} \qquad (15)$$

The strain rate at the maximum stress is given by $\dot{e} = \tau_{\max}^n$; the strain-rate at the minimum stress is $\dot{e} = \tau_{\min}/R_\mathrm{m}^m = \tau_{\min}^{1+m\alpha/b}/\mathsf{R}_\mathrm{m}^m$. Equation (15) shows that the stress extrema are both decreasing functions of the damage:healing ratio $q\mathcal{D}/C$ at least for the choice of parameters in this study (i.e., $q = b = 4$, $n = m = 3$ and $0 \le \alpha \le 8/3$).

3.2.1. *Some Earth-like numbers*

To put the stress limits and associated strain-rates on the hysteresis loop rheology (Figure 3, left column) into rough geological context, we consider a typical tectonic stress scale $\tau_\circ = 100$MPa (e.g., due to modest slab pull; see Forsyth and Uyeda, 1975; Hager and O'Connell, 1981; Bercovici et al., 2015a) and use the rheology for dry olivine from (Hirth and Kohlstedt, 2003; Rozel et al., 2011) at $T = 1000$K and pressure $P = 1.5$GPa. We also use $f = 10^{-3}$, $q = b = 4$, $m = n = 3$ and employ the coarsening numbers used previously (Bercovici and Ricard, 2014; Bercovici et al., 2015a), in which case the damage:healing ratio is $q\mathcal{D}/C \approx 4 \times 10^7$. Using $\alpha = 0$ and $\mathsf{R}_\mathrm{m} = 10^{-2}$, then $\tau_{\max} = 1.07$ and $\tau_{\min} \approx 0.022$ corresponding to dimensional stresses of 107 MPa and 2.2 MPa. The dimensionless strain-rates associated with these stresses are $\dot{e} = 1.22$ and $\dot{e} = 22{,}400$. With the chosen parameters, the strain-rate scale is very small, $\dot{\mathsf{E}} = 1.6 \times 10^{-18}\mathrm{s}^{-1}$, and thus the dimensional strain-rates are $2 \times 10^{-18}\mathrm{s}^{-1}$ and $4 \times 10^{-14}\mathrm{s}^{-1}$ (corresponding to shear velocities of 6.3 μm/yr and 12.6 cm/yr, respectively, across a 100 km wide deformation belt). This implies that if the medium (i.e., the lithosphere) is weakly deforming on the *creeping* branch with a tectonic stress of around 100MPa, then a small sustained increase in stress above 107MPa will make it go unstable and eventually jump to the *mylonite* branch with high strain-rates and localization. If the stress is then slowly (i.e., quasi-statically) reduced, the medium will stay on the *mylonite* branch until it reaches a stress of about 2MPa, and then will necessarily have to jump back to the *creeping* branch with extremely slow deformation. In short, it does not take much of a stress increase to jump from a the nearly rigid *creeping* branch to the localized *mylonite* branch, and once on that weak branch, it takes a large reduction in stress to leave the *mylonite* branch and return to the *creeping* state.

For choices of $\alpha > 0$, the stress maximum changes very little from that for $\alpha = 0$, but the minimum stress

changes considerably. For the case of $\alpha = 8/3$, the approximate solutions give maximum and minimum dimensionless stresses of 1.4 and 1.1×10^{-5}, with associated strain-rates of 2.7 and 1.4×10^{-9}, respectively (see Figure 3). For a 100MPa stress scale, these dimensionalize to stress extrema of 140MPa and 1.1kPa, associated with strain-rates of $4 \times 10^{-18}\mathrm{s}^{-1}$ and $2 \times 10^{-27}\mathrm{s}^{-1}$. Thus the jump from *creeping* to *mylonite* branches occurs at a similar stress and strain-rate as with the $\alpha = 0$ case above, but the jump back from the *mylonite* to *creeping* state occurs at such extremely low stress and strain-rates that it might never occur in a tectonic environment.

The dimensionless roughness associated with the stress maxima is approximately $r = 1$ for all cases since this occurs on the field boundary R_f; the roughness for the minimum stresses are $r = \mathsf{R}_\mathrm{m} = 10^{-2}$ for $\alpha = 0$ and $r = 20$ for $\alpha = 8/3$. These quantities can be dimensionalized to a grain-size by the scale $\pi\mathsf{R}/2$ (since $\pi/2$ is the typical ratio of grain-size to roughness; see Appendix A.2), which for the above stress, pressure and temperature conditions is about 350μm. For $\alpha = 0$, the grain-sizes on the *creeping* branch, are thus larger than 350μm, a size at which the maximum stress is reached. The grain-sizes on the *mylonite* branch, are smaller than 3.5μm, at which the minimum stress occurs. In the case of $\alpha = 8/3$, the *mylonite* , *intermediate* and *creeping* "piezometers" overlap in roughness r space between the extrema, and thus an observation of grain-size in that overlap could be interpreted as lying on any of these branches, although only the *mylonite* and *creeping* ones are stable. In this case, the *creeping* branch corresponds again to grain-sizes larger than 350μm; on the *mylonite* branch, however, the grain-size can become as large as 7 mm at extremely small stresses before the system jumps to the *creeping* branch in the dislocation creep regime.

3.3. Simple shear localization

In a simple shear system, where flow in a layer is only driven by relative motion of its boundaries, the velocity is given by $\mathbf{v} = u(y)\hat{\mathbf{x}}$, and hence the single stress component is the shear stress τ_{xy}, which conservation of momentum for creeping flow dictates is uniform across the layer. For most rheologies, strain-rate is a single-valued function of stress and thus a uniform stress leads to uniform shear and no localization within the layer, neglecting the potential effect of shear heating (Bercovici and Karato, 2003). If the rheology is classically velocity or shear-weakening, or pseudo-stick-slip (Whitehead and Gans, 1974; Bercovici, 1993; Bercovici and Karato, 2003) – such that beyond a given strain-rate the stress drops – then a given stress leads to the possibility of two states, a low strain-rate and high-strain-rate values, in which case shear-localization can occur; however the high-strain-rate state is unstable and keeps localizing indefinitely.

With our hysteretic model, three strain-rates are allowed, only one of which is unstable, and where the low- and high-strain-rate, or *creeping* and *mylonite* states, can stably coexist. This effect therefore allows localization that is both strong and stable, as can be readily demonstrated for the simple-shear system. Assuming that the shear is driven by the stress τ_{xy} and thus is also constant in time as well as uniform, then the characteristic stress scale is $\boldsymbol{\tau}_\circ = \tau_{xy}$ such that the dimensionless stress is $\tau = 1$. The governing dimensionless damage equation (8) thus becomes

$$\frac{\mathrm{d}r}{\mathrm{d}t} = \frac{C}{qr^{q-1}} - \mathcal{D}\frac{r^2\left(1 + r^{-m}\right)}{1 + (r/\mathsf{R}_\mathrm{m})^b} \tag{16}$$

which we can integrate numerically, and from it infer the shear rate given by (7) for the single component of strain-rate $\dot{e}_{xy} = \frac{1}{2}\mathrm{d}u/\mathrm{d}y$. If $r = r(y,t)$, representing evolving horizontal bands of variable grain-size, then the dimensionless velocity profile is simply

$$u(y,t) = 2\int_0^y (1 + r(\mathrm{y},t)^{-m})\mathrm{dy} \tag{17}$$

where we nondimensionalize distance y by the layer width L and thus $0 \le y \le 1$. We thus solve for the evolution of r, which then determines that of u.

For the numerical integration, we impose the initial condition $r = r_0 + \delta r(y)$ where r_0 is a constant and may or may not be one of the equilibrium roots. However, it is easiest to demonstrate the instability using r_0 for the *intermediate* unstable branch. In this case the grains at y where $r(y) > r_0$ will evolve to the large-grain, strong *creeping* state, while those where $r < r_0$ will evolve toward small-grain *mylonite* state. Eventually the system evolves from having nearly uniform shear, to a step-like profile with weakly deforming blocks separated by narrow bands of extreme shear (Figure 4). (However, note that if r_0 is chosen very close to the field boundary, which for this case is at $r = 1$, then the *creeping* branch is also unstable, and thus the entire layer would evolve to the *mylonite* state.)

The proximity of the initial condition to the stable branches (Figure 2a) is informative about how other initial conditions will evolve. For example, initial conditions outside the hysteresis loop will evolve to a stable uniform strain-rate state, on either the *creeping* branch (for very small $q\mathcal{D}/C$) or the *mylonite* branch (for very

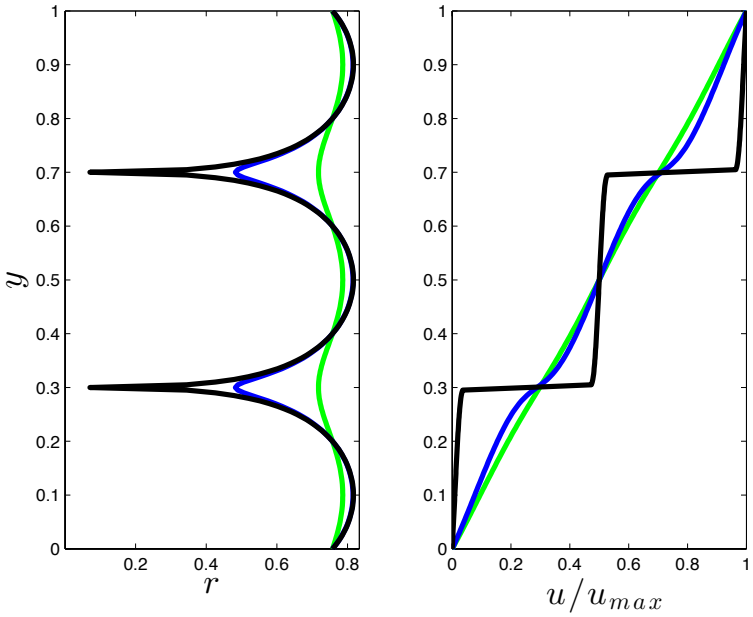

Figure 4: Evolution of profiles in roughness (or characteristic grain-size) r and velocity u across a layer subjected to simple shearing motion in the x direction, as described in §3.3. The calculation is specifically for $q = 4$, $\mathcal{D} = 100$, $C = 10^{-5}$ and hence $q\mathcal{D}/C = 4 \times 10^7$. The initial condition is that $r = r_0 + \epsilon \sin(ky)$ where r_0 is the *intermediate* unstable root shown in Figure 2 for the associated value of $q\mathcal{D}/C$ (specifically $r_0 = 0.758$), $\epsilon = 10^{-2}$ and $k = 5\pi$, given that $0 \le y \le 1$, and using 201 grid points in y. The calculation uses a basic MATLAB ordinary-differential equation solver to integrate (16) forward in time for each point in y. Three profiles are shown at dimensionless times $t = [0, 2.5345, 2.5684) \times 10^5$ for the green, blue and black curves respectively; since the calculation begins from an equilibrium root where $dr/dt = 0$ with a very small perturbation, the time to completely reach the stable solutions (where $dr/dt \to 0$) is in principle infinite; thus the time-scales involved are not geologically relevant. The velocity profiles are also normalized by the maximum dimensionless velocity u_{max}, and these are, in order of increasing time, $u_{max} = 6.6, 7.8$ and 64.8. Using a stress scale of 100MPa and associated strain-rate scale $\dot{\mathrm{E}} \approx 2 \times 10^{-18}\mathrm{s}^{-1}$ (see §3.2.1), and a typical length scale $L = 3 \times 10^6$m, these velocities are dimensionally about 0.1, 0.12 and 1 cm/yr, respectively; however, increasing the stress scale by a factor of 2 increases the velocities by a factor of 8. The narrow shear-zones at the final time step have dimensionless width of approximately 0.01, or using $L = 3 \times 10^6$m, are about 30km wide.

large $q\mathcal{D}/C$), and thus have no localization: i.e. the layer will either be uniformly strong with large grains or uniformly weak with small grains. If the initial condition is within the range of $q\mathcal{D}/C$ inside the hysteresis loop, and is anywhere between the stable branches, then r will evolve away from the unstable branch toward the nearest stable one. Thus, if for example, r_0 is on the *creeping* branch, but δr places r at a given position y on the other side of the unstable *intermediate* branch, then that location will evolve toward the *mylonite* branch and induce localization. Moreover, near the end of the *creeping* branch at large $q\mathcal{D}/C$, a small but finite perturbation to the r_0 on that branch will go unstable and evolve to the weak branch; obviously this just means at a higher damage:healing ratio, a strong *creeping* system is more prone to a localizing instability. Likewise, at the low $q\mathcal{D}/C$ end of the *mylonite* branch, a weak small-grain system is prone to a stiffening instability. Finally, if the stress is entirely removed (so that $\mathcal{D} = 0$) after the localized shear-bands develop, then only the *creeping* branch is available at $q\mathcal{D}/C = 0$, in which case the thin shear zones will slowly "heal" away (see the similar calculation in Bercovici and Ricard, 2012) and return the layer to its original uniform shear profile and homogeneous grain-size.

Without beating a dead-horse too much, the notion of proximity of branches is useful for one more interpretation. If the spatial perturbation to a uniform strong, large-grain system is caused by an inherited weak zone with small enough grains, then it will go unstable if that perturbation is large enough to place r on the other side of the unstable branch. Thus finite perturbations due to dormant and inherited weak zones (Bercovici and Ricard, 2014) will trigger new localization as soon as they pass into high enough stress state (i.e., where $q\mathcal{D}/C$ is large enough) to put them in the range of the hysteresis loop. A similar perturbation can also occur with exhumation and cooling, as will be discussed in the next section.

3.4. Some comparison to field observations

Despite our simplifying assumptions so far, the theoretical deformation maps in §3.2 invite an application and comparison to field observations of mylonites. Of greatest use are observations across shear zones that include both highly mylonitized samples and neighboring weakly deformed samples. Here, we consider two field studies, of Jin et al. (1998) and Linckens et al. (2011). Jin (1995) and Jin et al. (1998) provide a profile of measurements across a fault in the Balmuccia peridotite in the Ivrea zone massif, with detailed analyses of olivine grain-sizes both within an ultramylonite in the fault zone as well as outside the fault zone, which contains both large-grained mylonites, protomylonites and porphyroclasts. Measurements of lattice-preferred orientation (LPO), indicate that the larger-grain mylonite and clasts have a significant component of dislocation creep, while the ultramylonite zone has a weak and diffuse LPO signature indicative of greater diffusion creep. (Linckens et al., 2011) performed a comprehensive analysis of deformation microstructures in the Hilti massif mantle shear zone in the Oman (Semail) ophiolite (see also Tasaka et al., 2014). Although the samples are not in a profile across a fault they include a range of structures from large-grained porphyroclastic tectonites, protomylonites, mylonites and ultramylonites (see also Herwegh et al., 2011; Linckens et al., 2014, 2015). Measurements of LPO in these samples indicate that the larger-grain mylonites and clasts have a significant component of dislocation creep, while the ultramylonites essentially have no LPO signature, indicative of greater diffusion creep (see also Tasaka et al., 2014).

For each set of measurements, we adopt the grain-size data as is (see Appendix B and Table B.1). Experimental stress estimates are typically based on the correlation of stress to grain-size in one of the phases (usually olivine) using either an empirical paleopiezometer (e.g., Karato et al., 1980; Van der Wal et al., 1993; Stipp et al., 2010) or a paleowattmeter (Austin and Evans, 2007; Rozel et al., 2011), both of which are assumed to represent a balance of normal grain-growth with grain comminution during dynamic recrystallization, which only occurs in dislocation creep. However, the very small grain-sizes in mylonites and especially ultramylonites are typically in the diffusion-creep regime, and application of the paleopiezometer or paleowattmeter to these grain-sizes is problematic, and typically predicts unreasonably high stresses, approaching or exceeding that of rock strength (see also discussion by De Bresser et al., 2001; Linckens et al., 2011).

Here we use our model to estimate stresses for the measured grain-sizes using solutions to (11), or specifically employing the relations in (12) as approximate "paleowattmeters" (Figure 5; see also Appendix B for details on the comparison to field data). In general, the large-grained clasts always fall on the *creeping* branch (approximated by (12a)), the small-grained ultramylonites always fall on the *mylonite* branch (approximated by (12c)); the intermediate grain-sized mylonites and protomylonites fall either on the *intermediate* branch (12b) or the *mylonite* branch depending on the value of the parameter α defined in (10).

For both field studies we primarily consider a case for a moderate damage:healing ratio $q\mathcal{D}/C$. Since $q\mathcal{D}/C$ is temperature dependent, it has different values for each lithology in a given field area, thus we consider the case in which its reference value at a given reference temperature is moderate. We also assume R_{m} is parallel to the field boundary R_{f}, i.e., $\alpha = 8/3$, which allows the *creeping* branch to match the appropriate piezometer. (See Appendix B for more details as well as some other sample cases using different reference damage:healing ratios and values of α.)

For the parameters considered here, the mylonite grain-sizes (both proto- and ultra-mylonites) fall on the *mylonite* branch at lower stresses than for the large-grain clasts, by about an order of magnitude or more. The localization with formation of mylonites is not predicted to involve a huge increase in stress as inferred by the classic piezometer (see comparison curves in Fig. 5), but instead a drop or little change in stress.

That the protomylonites fall on the *mylonite* branch at low stresses is an artifact of these branches being steady state solutions, since the protomylonites are likely transient features (Linckens et al., 2011); i.e., if their grain-sizes were fixed then the stress would eventually evolve to the steady-state low value, but if the stress is fixed or altered slowly by external driving forces (namely tectonic stresses) then the protomylonite grain-sizes would be transitory and evolve toward the ultramylonite state on the stable *mylonite* branch. Indeed even the ultramylonites might be transient if they were evolving to smaller sizes at larger stresses, comparable to the original stress of the clasts, but were frozen in once they were fully exhumed. Either way, mylonitization is predicted to evolve at a more uniform stress rather than by giant spikes in stress.

For each field area the temperature is inferred to have decreased in the process of grain-size reduction, which possibly induced chemical reactions and nucleation of small grains that helped drive mylonitization (Linckens et al., 2011). Such recrystallization and nucleation

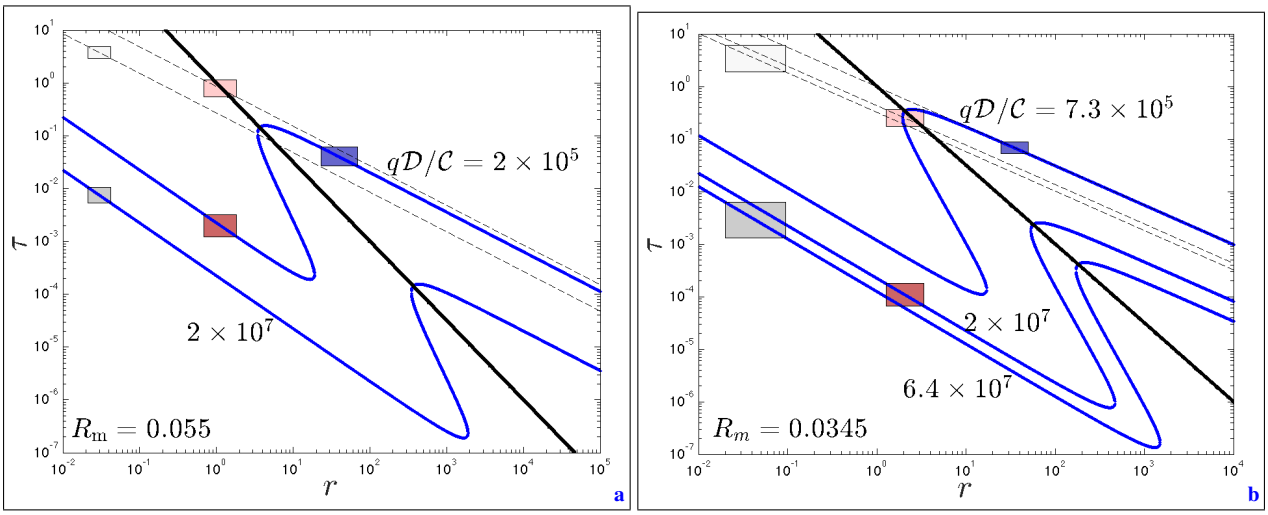

Figure 5: Application of theoretical deformation maps to data from (Jin, 1995; Jin et al., 1998) (a) and (Linckens et al., 2011) (b), as summarized in Table B.1. Only a sample case is shown in which $\alpha = 8/3$ and for modest damage partitioning f. (More specifically, since $f = f(T)$, the case considered is for when $f(1000\text{K}) = 10^{-3}$). The two curves in frame (a) are for $T = 1200°\text{C}$ (associated with the large-grained clasts, indicated by the blue box, and normal and proto-mylonites, red boxes), and 800°C (for the ultramylonites, light grey boxes), which correspond to the smaller and larger values of $q\mathcal{D}/C$, respectively. The three curves in frame (b) are for $T = 1100°\text{C}$ (clasts; blue box), 800°C (proto-mylonites; red boxes) and 700°C (ultra-mylonites; light gray boxes), corresponding to the sequentially increasing $q\mathcal{D}/C$, respectively. $\mathsf{R}_{\rm m}$ (indicated on each frame) is chosen so that the stresses inferred for the large-grain porphyroclasts (blue boxes) on the *creeping* branch match the piezometrically inferred stresses (see Table B.1), using a dimensionalizing stress scale of $\tau_\circ$ =100MPa. We also show for comparison the approximate paleo-wattmeter curves (dashed lines) and their predicted stresses for the mylonite data (lighter shaded boxes on the dashed lines); the approximate paleo-wattmeter is given by $C_i/(p\mathcal{R}^{p-1}) = \mathcal{D}\mathcal{R}^2\tau^{n+1}$ where C_i is the grain-coarsening rate, $\mathcal{R}$ is grain-size and $p = 2$; to let this approximately match the *creeping* branch (12a) for the highest temperature large-grain porphyroclast data, we assume $C_i \approx (p/q)(\pi/2)^{p+1}C/\mathsf{R}_{\rm m}^b$ which is much larger than C as expected (Bercovici and Ricard, 2012, 2013). Note that the Jin (1995) grain-size for the large-grained porphyroclasts is only one number (see Table B.1), but here we arbitrarily assume a range of ±50% around this value to make the displayed box visible. See §3.4 and Appendix B for further explanations.

would likely be influenced by the presence of distributed and diminished pinning bodies since they tend to increase the chemical potential of larger grains (Bercovici and Ricard, 2012), whose reduction by any means (be it diffusion or reactions) would relieve chemical potential differences and restore thermodynamic equilibrium. Our model however simply implies that a drop in temperature acts as a perturbation that drives the system off of the stable *creeping* branch to the stable *mylonite* branch. In particular, if the modest stress on the large-grain clasts residing on the *creeping* branch were held fixed (or slowly varied by external tectonic forces) during cooling, then the only other stable branch available after a sufficient temperature drop is the *mylonite* branch, to which the grains necessarily evolve.

In the end, our model suggests that measurements in and around mylonites should fall or converge on two stable trends on a deformation map, not simply on one paleopiezometer or paleowattmeter trend that may or may not be applied appropriately. Indeed, the piezometer or wattmeter lines correspond to the *creeping* branch that is confined to the dislocation creep regime for coarse grains. The fully-formed mylonites, that have reached the end stage in their grain-size evolution as ultramylonites, would fall on the stable *mylonite* curve, which represents a different piezometer than the classical relation since it only applies to the diffusion creep regime; indeed, this piezometric equilibrium is not controlled by the density of dislocations in each phase but by the pinning effect that each phase exerts on the other phase. Transitional forms like protomylonites would fall on the *mylonite* branch only if their grain-sizes were fixed and the stresses allowed to relax to steady state, otherwise they are unstable. The theoretical model also predicts that the classical dislocation-creep piezometer curves would never cross the field boundary into diffusion creep; it is instead truncated by a peak stress at the field boundary, and this peak represents an effective yield criterion beyond which the system transitions to a mylonite or ultramylonite with high strain-rates. Likewise, the *mylonite* branch has a low-stress truncation, below which mylonites would not be stable and would necessarily undergo grain-growth to the coarse-grained *creeping* branch or piezometric line.

4. Discussion and Conclusion: Plate tectonic states

Our basic model for grain-damage and pinning in polycrystalline rocks provides a frame-work for understanding lithospheric shear weakening and plate-generation, and is consistent with laboratory and field observations of permanent diffusion creep in mylonites (e.g., Bercovici and Ricard, 2012). With the modification proposed here, which allows for hysteresis, we also provide an interpretation of field data on mylonites that predicts only moderate changes in stress during mylonitization rather than the enormous stress increases inferred by the physically inconsistent application of classic piezometers.

Our hysteretic grain-damage model also predicts that a plate-tectonic regime exists when the physical conditions (stress, temperature, etc.) permit two stable coexisting deformation states for a given stress, i.e., a slowly deforming rigid state analogous to a strong plate interior, and a rapidly deforming state akin to shear-localization on a plate boundary. Needless to say, stress is not homogeneous on Earth, and indeed plate-like behavior can be obtained with grain-damage even without hysteresis; in this case, the plate-like and plate-boundary-like states depend entirely on the heterogeneity of the convectively imposed stress, at least initially, since once a weak-zone develops, it influences the stress heterogeneity itself (Bercovici and Ricard, 2014). However, grain-damage with hysteresis provides localization even without stress heterogeneity and thus allows localization to develop spontaneously rather than depending on the spatial structure of the convective driving force.

The hysteresis effect also has an advantage over traditional shear-localization schemes which propose that stress drops away indefinitely once beyond a peak value (e.g., Bercovici, 1993, 1995); this only leads to an unstable behavior that runs away to zero-thickness localization zones (Tackley, 1998, 2000), and would be the equivalent of our models unstable branch (for $\alpha < 4/3$). With grain-damage hysteresis, shear-localization evolves to a stable *mylonite* branch that limits the narrow thickness and high strain-rate of the localized zone.

We can also apply grain-damage hysteresis to qualitatively compare terrestrial planets, especially Earth and Venus. Given a conservative convective stress and mid-lithosphere temperatures for Earth and Venus, we can estimate a range of values for the damage:healing ratio $q\mathcal{D}/C$ for both planets (Figure 6). Earth likely resides well inside the hysteresis loop and thus can maintain two stable deformation branches representing strong plates and rapidly deforming plate boundaries. Even if Earth like conditions allowed only the strong *creeping* branch, sufficient perturbations in strength or stress, such as might happened by lithospheric drips, cooling by exhumation, or even a large enough meteorite impact, could tip the system locally toward the *mylonite* or plate-boundary branch, which would also be stable. Venus, on the other hand, appears to reside near the truncation of the *mylonite* branch beyond which the *creeping* semi-rigid branch is the only stable state available. However, Venus might straddle this end-point allowing perturbations to reach the *mylonite* branch and plate-boundary formation. But, since the *mylonite* branch near this end-point is so close to the unstable *intermediate* branch, it would be more unstable to perturbations that would return it to the *creeping* branch and stagnant-lid behavior. Such brief forays into the *mylonite* branch would be manifest as episodic behavior whereby tectonic behavior is transient, while stagnant lid behavior is more persistent. Although this is a very qualitative comparison and subject to significant uncertainty in the chosen parameters, it shows that grain-damage hysteresis is potentially a powerful concept with which to understand plate-tectonic states on Earth and other planets.

While only a minor adjustment to the grain-damage theory leads to hysteretic behavior, the specific modification is a simple parameterization of variations in interface damage due to its suppression at larger grain-sizes and interface roughness because of the predominance of dynamic recrystallization, and then an increase in interface damage to enhanced inter-grain mixing at smaller grain-size and roughness. However, the microphysical mechanisms behind such transitions in interface damage are not articulated in this model, and thus require further elaboration and investigation.

Appendices

Appendix A. Grain-damage model: theoretical considerations

The coupled evolution equations for interface roughness r and grain-sizes $\mathcal{R}_i$ in each phase i of a rock mixture (e.g., in a peridotite, where pyroxene is the minor phase $i = 1$, and olivine is phase $i = 2$) are, as given by Bercovici and Ricard (2012) (see also Bercovici and Ricard, 2013, 2014; Bercovici et al., 2015a),

$$\frac{\mathrm{d}r}{\mathrm{d}t} = \frac{\eta G}{q r^{q-1}} - \frac{r^2}{\eta\gamma} f_1 \overline{\Psi} \tag{A.1}$$

$$\frac{\mathrm{d}\mathcal{R}_i}{\mathrm{d}t} = \frac{G_i}{p\mathcal{R}_i^{p-1}}\mathcal{Z}_i - \lambda\frac{\mathcal{R}_i^2}{3\gamma_i} f_G \Psi_i \mathcal{Z}_i^{-1} \tag{A.2}$$

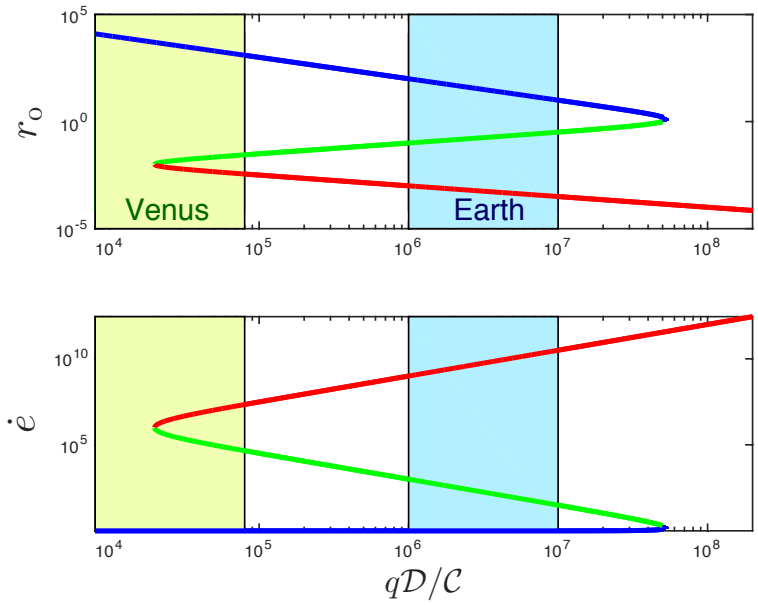

Figure 6: Comparison of hysteresis curves vs planet ranges of $q\mathcal{D}/C$, for both Earth (light blue) and Venus (olive green) for both grain-size and strain-rate (both dimensionless). The colors of the hysteresis branches are the same as in Figure 2. Experimental data, largely for dry olivine, are used to calculate $q\mathcal{D}/C$ as described in §2.3. With that data, the calculations are based on using a modest stress scale for Earth of $\boldsymbol{\tau}_\circ = 10$MPa, a mid-lithosphere temperature $T = 1000$K and damage fractions $f = 10^{-4} - 10^{-3}$. For Venus we use $T = 1300$K, a value of $\boldsymbol{\tau}_\circ$ reduced by 10 (Lenardic et al., 2008; Landuyt and Bercovici, 2009b; Foley et al., 2012) and we employ $f(T) = f_0 \exp(-2(T/1000)^{2.9})$ inferred by Rozel et al. (2011).

where G_i and G are coarsening coefficients for the grains and interface, respectively, p and q are constant exponents (typically $p = 2$ and $q = 4$), $\eta \approx 3\phi_1\phi_2$ in which ϕ_i is the phase volume fraction (such that $\sum_i \phi_i = 1$), γ and γ_i are the interface and grain-boundary surface tensions, respectively (typically we assume $\gamma_i = \gamma$), Ψ_i is the rate of deformational work on phase i and $\overline{\Psi} = \sum_i \phi_i \Psi_i$, and

$$\mathcal{Z}_i = 1 - \mathfrak{c}(1-\phi_i)\frac{\mathcal{R}_i^2}{r^2} \tag{A.3}$$

is the Zener pinning factor, in which $\lambda = 4.95$ and $\mathfrak{c} = 0.87$ for the grain-size distribution used by Bercovici and Ricard (2012, 2013, 2014); Bercovici et al. (2015a). The rheology is given for each phase i such that

$$\underline{\dot{\boldsymbol{\epsilon}}} = (\mathsf{A}_i \tau_i^n + \mathsf{B}_i/\mathcal{R}_i^m)\underline{\boldsymbol{\tau}}_i \tag{A.4}$$

where A_i and B_i are the dislocation and diffusion compliances for each phase, n and m are as described in the main text, and $\tau_i^2 = \frac{1}{2}\underline{\boldsymbol{\tau}}_i : \underline{\boldsymbol{\tau}}_i$ is the 2nd invariant of the stress tensor $\underline{\boldsymbol{\tau}}_i$. With this rheology $\Psi_i = \underline{\dot{\boldsymbol{\epsilon}}} : \underline{\boldsymbol{\tau}}_i = 2(\mathsf{A}_i\tau_i^{n+1} + \mathsf{B}_i\tau_i^2/\mathcal{R}_i^m)$. Lastly, the partitioning fractions of deformational work going toward interface and grain-boundary energy are f_I and f_G, respectively, although here we deviate slightly from the definitions described by Bercovici and Ricard (2012). In particular, we now prescribe that the total fraction of work going to surface energy, both interface and grain boundary, is $f_\mathrm{I} + f_\mathrm{G}$, while that going to dissipative heating is $1 - f_\mathrm{I} - f_\mathrm{G}$; this differs slightly from our prior definitions of partitioning fractions, but without loss of generality and makes the following development simpler.

As described by Rozel et al. (2011) and Bercovici and Ricard (2012) the fraction of work going toward grain-boundary damage is assumed to be restricted to dislocation creep (i.e., is caused by dynamic recrystallization; see Karato et al. (1980); Karato (2008)), which implies that $f_\mathrm{G}\Psi_i = 2f\mathsf{A}_i\tau_i^{n+1}$ and thus

$$f_\mathrm{G} = \frac{f\mathcal{R}_i^m}{\mathcal{R}_f^m + \mathcal{R}_i^m} \tag{A.5}$$

where f is a maximum partitioning fraction and $\mathcal{R}_f = (\mathsf{B}_i/(\mathsf{A}_i\tau_i^{n-1}))^{1/m}$ is the grain-size at the field-boundary (i.e., the transition from dislocation to diffusion creep). The simplified model used in the main text assumes a pinned state (for an imposed r, $\mathcal{R}_i$ evolves toward $\mathcal{Z}_i \approx 0$) wherein, for a peridotitic mixture ($\phi_1 \approx 0.4$), $\bar{\mathcal{R}} = \sum_i \phi_i \mathcal{R}_i \approx \frac{\pi}{2} r$ and that the rheology depends on this roughness r, provided the compliances of the phases are comparable (see (3) and also Appendix A.2); in

this case, the field boundary roughness is denoted by $R_\mathrm{f} = \frac{2}{\pi}\mathcal{R}_f$.

In Bercovici and Ricard (2012, 2013, 2014); Bercovici et al. (2015a), f_I was assumed constant, which implied that interface damage would occur regardless of deformation mechanism. However, here, and as described in §2.1, we allow f_I to be variable such that interface damage is partially suppressed whilst other sinks of deformational work are available, including viscous dissipation and grain-boundary damage in dislocation creep while grains and the interface are moderately coarse. In this case we prescribe a similar relation to (A.5):

$$f_\mathrm{I} = f\frac{R_\mathrm{m}^b + \chi r^b}{R_\mathrm{m}^b + r^b} \tag{A.6}$$

where b is a constant exponent, $\chi < 1$ and prescribes the minimum partitioning fraction $f_\mathrm{I} = \chi f$ at large r, and R_m is an interface roughness scale above which damage is suppressed, and below which interphase/inter-grain mixing (which is a manifestation of interface distortion and damage that also disperses Zener pinning bodies) becomes more effective. For simplicity (and lack of knowledge otherwise), we assume both f_I and f_G approach the same maximum value of f. For most of the analysis (e.g., in the main text), we assume $\chi \approx 0$ for simplicity, although we present some discussion of cases with $\chi > 0$ in Appendix A.3. As discussed in the main text (§2.1), we assume $R_\mathrm{m} < R_\mathrm{f}$, and that R_m, like R_f, is a function of stress and is potentially parallel to R_f (see §2.2). Finally we note that $R_\mathrm{m} < R_\mathrm{f}$ is a necessary (though not sufficient) condition for hysteresis (the value of b is also constrained for hysteresis to exist; see §3.1); in the case that $R_\mathrm{m} = R_\mathrm{f}$, $b = m$, and $\chi = 0$, such that $f_\mathrm{I} + f_\mathrm{G} = f$ then hysteresis can be easily shown to never exist by following the simple system presented in the main text (again, see §2.4.1).

Appendix A.1. Hysteresis in the full grain-damage model

In the main text we consider only the governing equations in the pinned-state limit of $\mathcal{Z}_i \approx 0$ (see Appendix A.2), which yields a simple system of equations that illustrates the basic hysteresis effect. However, if interface damage is suppressed at large values of r and $\mathcal{R}_i$, then the pinned-state is possibly a weak assumption in the *coarse-grained* limit. Thus here we test whether hysteresis exists for the complete system of equations to ensure it does not only exist by virtue of the pinned-state assumption.

To nondimensionalize the full governing equations we choose a stress scale $\boldsymbol{\tau}_\circ$, a grain scale $\mathsf{R} = (\bar{\mathsf{B}}/(\bar{\mathsf{A}}\boldsymbol{\tau}_\circ^{n-1}))^{1/m}$ (which is slightly different than the roughness scale defined in (6) for the simpler model, by a factor of approximately $\pi/2$; see Appendix A.2) and strain-rate scale $\dot{\mathsf{E}} = \bar{\mathsf{A}}\boldsymbol{\tau}_\circ^n$, where any averaged quantity is defined as $\bar{Q} = \sum_i \phi_i Q_i$. This leads to the dimensionless governing equations

$$\frac{\mathrm{d}r}{\mathrm{d}t} = \frac{C}{qr^{q-1}} - \mathcal{D}r^2\omega\sum_i \phi_i\left(\mathsf{a}_i\tau_i^{n+1} + \frac{\mathsf{b}_i\tau_i^2}{\mathcal{R}_i^m}\right) \tag{A.7}$$

$$\frac{\mathrm{d}\mathcal{R}_i}{\mathrm{d}t} = \frac{C_i}{p\mathcal{R}_i^{p-1}}\mathcal{Z}_i - \mathcal{D}_i\mathcal{R}_i^2\mathsf{a}_i\tau_i^{n+1}\mathcal{Z}_i^{-1} \tag{A.8}$$

where $\mathsf{a}_i = \mathsf{A}_i/\bar{\mathsf{A}}$ and $\mathsf{b}_i = \mathsf{B}_i/\bar{\mathsf{A}}$,

$$C = \frac{\eta G}{\mathsf{R}^q\bar{\mathsf{A}}\boldsymbol{\tau}_\circ^n} \quad \text{and} \quad \mathcal{D} = \frac{2f\mathsf{R}\boldsymbol{\tau}_\circ}{\gamma_1\eta} \tag{A.9a}$$

$$C_i = \frac{G_i}{\mathsf{R}^p\bar{\mathsf{A}}\boldsymbol{\tau}_\circ^n} \quad \text{and} \quad \mathcal{D}_i = \frac{2\lambda f\mathsf{R}\boldsymbol{\tau}_\circ}{3\gamma_i} \tag{A.9b}$$

$\mathcal{Z}_i$ is still as defined in (A.3), and $\omega = f_\mathrm{I}/f$ as defined in (A.6) except that now R_m is nondimensionalized by R.

Here we only consider whether the full equations allow hysteresis for a given stress, as in §3.1. We thus assume that the given stress is the same across all phases and given, dimensionally, by $\boldsymbol{\tau}_\circ$ such that the dimensionless stress is $\tau_i = 1$. Moreover, we assume the phases have similar rheologies in which case $\mathsf{a}_i = \mathsf{b}_i \approx 1$. The steady damage equations become

$$\omega_0 r_0^{q+1}\left(1 + \sum_i \frac{\phi_i}{\mathcal{R}_{i0}^m}\right) - \frac{C}{q\mathcal{D}} = 0 \tag{A.10a}$$

$$\mathcal{R}_{i0}^{p+1} - \frac{C_i}{p\mathcal{D}_i}\mathcal{Z}_{i0}^2 = 0 \tag{A.10b}$$

where $\omega_0 = \omega(r_0)$, $\mathcal{Z}_{i0} = \mathcal{Z}_i(\mathcal{R}_{i0}, r_0)$. The most reliable numerical solution method for these three coupled polynomials is to use an initial "guess" value of r_0 in (A.10b) to obtain estimates of $\mathcal{R}_{i0}$ for both $i = 1, 2$; these $\mathcal{R}_{i0}$ are then used to solve (A.10a) for an estimate of r_0, which is averaged with the initial r_0 for an updated "guess", and then the iteration repeated till convergence. There are typically two pairs of real roots for $\mathcal{R}_{i0}$ and for each of these pairs there are three real roots for r_0, but when all are mapped out they display the hysteresis curves similar to the simpler system discussed in the main text (Figure A.1).

The stability of these roots is inferred by substituting the linear expansion given by

$$r = r_0(1 + \epsilon\mathsf{u}) \quad \text{and} \quad \mathcal{R}_i = \mathcal{R}_{i0}(1 + \epsilon\mathsf{v}_i) \tag{A.11}$$

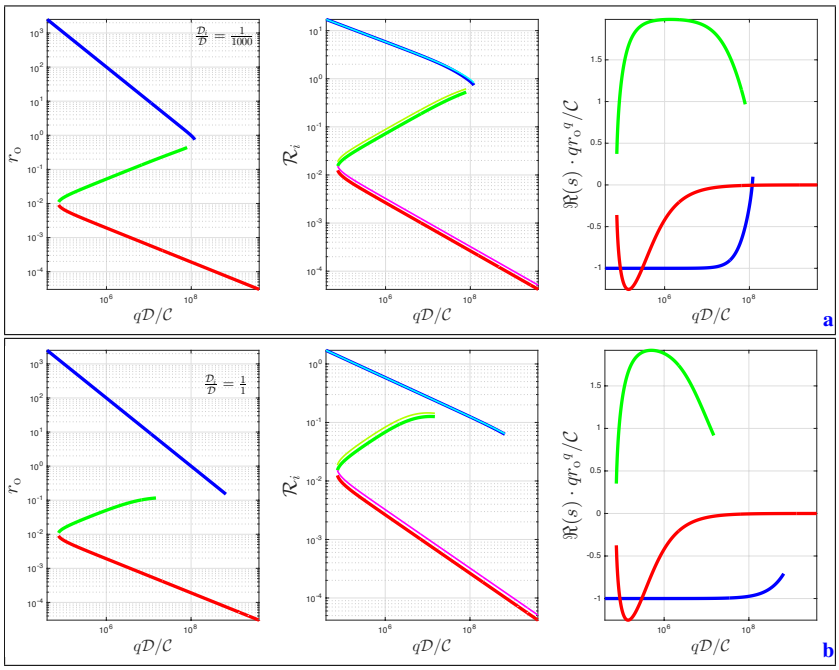

Figure A.1: Equilibrium states for r_0 and $\mathcal{R}_i$ from (A.10) and the maximum real growth rates for each root, from the solution to (A.12). The colors of the branches have the same association as in Fig 2; the thin cyan, olive and magenta curves on the plot for $\mathcal{R}_i$ are for $i = 2$. The two cases shown (a and b) are for different ratios of damage numbers, as indicated. For all cases $C_i = 1$ and $C_i = 10^{-5}$, $\mathsf{R}_\mathrm{m} = 10^{-2}$, $p = 2$ and, as in the main text, $q = b = 4$, $m = n = 3$.

into (A.7) and (A.8) leading to

$$\dot{\mathsf{u}} = -\frac{C}{q r_0^q}\left((q+1-b(1-\omega_0))\mathsf{u} - m\sum_i \Lambda_i \mathsf{v}_i\right) \tag{A.12a}$$

$$\dot{\mathsf{v}}_i = -\frac{C_i \mathcal{Z}_{i0}}{p\mathcal{R}_{i0}^p}\left((p+1+\zeta_i)\mathsf{v}_i - \zeta_i \mathsf{u}\right) \tag{A.12b}$$

where

$$\Lambda_i = \frac{\phi_i/\mathcal{R}_{i0}^m}{1+\sum_i \phi_i/\mathcal{R}_{i0}^m} \quad \text{and} \quad \zeta_i = \frac{4\mathfrak{c}(1-\phi_i)\mathcal{R}_{i0}^2/r_0^2}{\mathcal{Z}_{i0}} \tag{A.13}$$

Assuming $\mathsf{u}, \mathsf{v}_i \sim e^{st}$, then (A.12) leads to a cubic characteristic equation for s, the maximum real root of which represents the maximum growth rate s_{max}; the fastest growth shows that small and large grain branches of the hysteresis loops are stable ($s_{max} < 0$) while the intermediate branch is unstable ($s_{max} > 0$) (see Figure A.1).

While the full solutions are slightly more complex than with the simplifying pinned-state assumption, the hysteresis curve for the equilibrium states and their stability are qualitatively the same. In particular, the slopes of the stable *creeping* and *mylonite* branches are very similar to that of the simpler pinned-state model (Figure 2), and even the truncation or bifurcation point at large $q\mathcal{D}/C$ for the *creeping* branch is approximately the same as in the simpler model. The *intermediate* branch shape and extent is more affected by relaxing the pinned-state assumption but it is an unstable branch anyway. The most notable effect of relaxing the pinned-state assumption is on the bifurcation point for the *mylonite* branch, which occurs at a value of $q\mathcal{D}/C$ about 4 times larger than for the simplified model. Since pinning governs the nature of the *mylonite* branch (i.e., pinning holds grains in "permanent" diffusion creep wherein they are most affected by self-softening and damage feedbacks), then an increase in r with decreasing $q\mathcal{D}/C$ weakens the pinning effect and eventually eliminates the *mylonite* branch; thus the pinned-state assumption over-estimates the effectiveness of pinning at larger r and thus leads to a less precise location of the *mylonite* branch truncation, although it is only off by a factor of 4. The most interesting implication for this is that the range of values of $q\mathcal{D}/C$ for Venus (Figure 6) falls even further outside the hysteresis loop, where its lithosphere would be even more dominated by rigid or sluggish behavior characterized by the *creeping* branch.

Appendix A.2. The pinned-state and simplified governing equations

As discussed previously (Bercovici and Ricard, 2012, 2013, 2014; Bercovici et al., 2015a) Zener pinning restricts grain-growth and for many systems the grain-size reaches a pinned-state wherein $\mathcal{Z}_i \approx 0$ (see Hiraga et al., 2010; Bercovici and Ricard, 2012); in this case, the grains are slaved to the evolution of the roughness r such that

$$\mathcal{R}_i \approx r/\sqrt{\mathfrak{c}(1-\phi_i)} \tag{A.14}$$

and then the only evolution relation is that of the interface given by (1) or (A.1). The rheology is still a composite of dislocation and diffusion creep but now takes the form shown in (3). However, in (3) , while $A \equiv \mathsf{A}_i$, B differs from B_i because we have replaced the grain-size dependence in diffusion creep with dependence on r. Using (A.14) the effective diffusion creep compliance absorbs a proportionality factor of order $(\pi/2)^m$ for $\phi_1 = 0.4$ for a peridotite and $\mathfrak{c} = 0.87$. This proportionality factor holds regardless of whether we use a simple volume averaged grain-size $\bar{\mathcal{R}} = \sum_i \phi_i \mathcal{R}_i \approx \frac{\pi}{2} r$, or more accurately a rheologically averaged grain-size $\bar{\mathcal{R}} = (\sum_i \phi_i/\mathcal{R}_i^m)^{-1/m} = 1.54r$. With these relations, the interface damage equation becomes (1) or more precisely (4). Moreover, since the constitutive law (3) is with respect to r, the field boundary grain-size $\mathcal{R}_f$ and field-boundary roughness R_f also differ by a factor of approximately $\pi/2$.

Appendix A.3. Effect of small, finite interface damage at large r (i.e., $\chi > 0$)

The fraction of deformational work going toward interface damage f_I is given by (2), as described in §2.1, according to which $f_\mathrm{I} \to \chi f$ as $r \to \infty$. In most of the analysis of this paper we assue $\chi = 0$, but here we consider the effect of relaxing that assumption and allowing $\chi > 0$. We simply wish to examine the effect of $\chi > 0$ on the hysteresis branches, and thus we only treat the case for a given stress, such that the dimensionless stress is $\tau = 1$. In this case, the interface roughness evolution equation (8) only changes with the definition of f_I, and thus the equilibrium balance of interface healing and damage becomes

$$0 = \frac{C}{qr^{q-1}} - \mathcal{D}r^2\left(1 + r^{-m}\right)\frac{1+\chi(r/\mathsf{R}_\mathrm{m})^b}{1+(r/\mathsf{R}_\mathrm{m})^b} \tag{A.15}$$

For $q = b = 4$ and $m = 3$ this is a 9th order polynomial in r, which can be solved numerically, but never displays more than three real roots for the parameter regimes considered in this paper, as in the original problem with $\chi = 0$. Approximate analytic solutions to these branches can be inferred, similarly to how (12) is obtained; however, we leave aside this analysis since the numerical solution to (A.15) is sufficient for our purposes. The stability of these equilibrium solutions can be determined, as is done in §2.4.2, which leads to perturbations with exponential growth rate

$$s = -\frac{C}{qr_0^q}\left[q + 1 - \frac{m}{1+r_0^m} - b\left(\frac{(r_0/\mathsf{R}_\mathrm{m})^b}{1+(r_0/\mathsf{R}_\mathrm{m})^b} - \frac{\chi(r_0/\mathsf{R}_\mathrm{m})^b}{1+\chi(r_0/\mathsf{R}_\mathrm{m})^b}\right)\right] \tag{A.16}$$

where r_0 is the solution to (A.15)

The effect of $\chi > 0$ is to reduce the range of hysteresis, i.e., wherein there are three co-existing roots, since clearly for $\chi = 1$ there is no suppression of interface damage and $f_\mathrm{I} = f$ for all r. For $\chi \ll 1$ there are still three distinct hysteresis branches, essentially the same as the case for $\chi = 0$ (Fig A.2). The stability of these three branches are also similar to the $\chi = 0$ case. One notable and not unexpected difference for these cases is that even for very small χ, the growth-rate for perturbations to the *creeping* branch are significantly bigger than for $\chi = 0$. This difference occurs because for large r, not only is the damage completely suppressed for $\chi = 0$, but the healing or coarsening rate is also extremely small since it goes as $1/r^q$. For $\chi > 0$, even if it is very small, the damage rate is finite and thus allows perturbations to the *creeping* branch to evolve much faster than if the damage rate vanishes. Overall the effect of $\chi > 0$ is unremarkable, however, allowing a small finite interface damage rate at large r will be useful for implementation of this theory in lithospheric and mantle flow models. Specifically, for models starting out with coarse-grained strong lithospheres, the interface damage rate may initiate with such astronomically small values if $\chi = 0$ that the model will not evolve localized deformation zones in sufficient time; allowing $\chi > 0$, even if $\chi \ll 1$, will help mitigate this difficulty.

Appendix B. Details on comparison to field data

The comparison of theoretical deformation maps to field observations in §3.4 uses data from the studies of Jin (1995); Jin et al. (1998) on the Balmuccia peridotite in the Ivrea zone massif, and Linckens et al. (2011) on the Hilti massif mantle shear zone in the Oman (Semail) ophiolite. Both studies analyzed a range of lithologies including large-grained porphyroclastic tectonites, protomylonites, mylonites and ultramylonites. The grain-size data with the inferred temperatures of the various

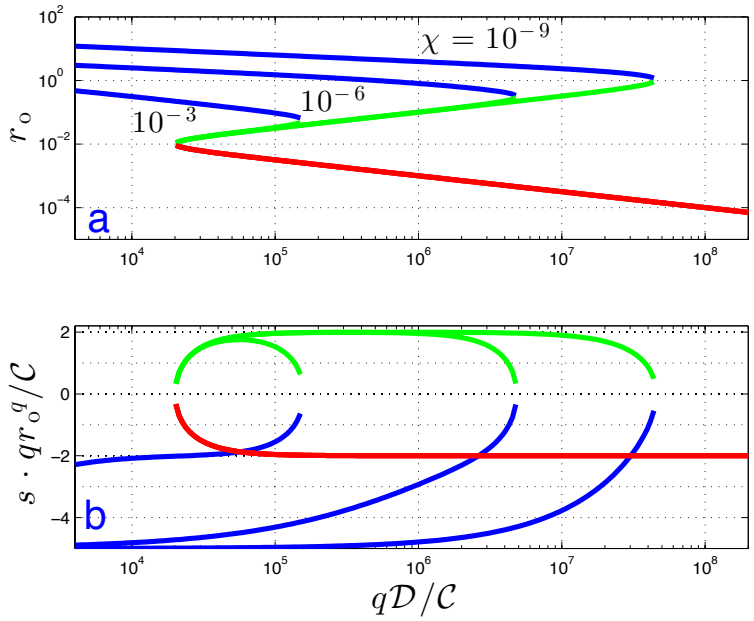

Figure A.2: Equilibrium states (a) and their growth rates and stability (b) for the case where interface damage reaches a finite asymptotic value rather going to zero as $r \to \infty$, as described in Appendix A.3. Parameters and curves are the same as in Fig. 2 except for the values of χ as indicated.

lithologies at their time of formation are summarized in Table B.1.

Although the data for each unit are inferred to be associated with different temperatures, we normalize the measured grain-sizes by using a stress scale $\tau_\circ$ = 100MPa, from which we obtain the roughness scale R from (6) for each temperature using the rheological data of Hirth and Kohlstedt (2003), and assuming for simplicity just one lithostatic pressure of P = 1.5GPa, corresponding to a depth of 50km. (The choice of $\tau_\circ$ is arbitrary and has no effect other than providing a characteristic tectonic stress scale; any choice of stress unit leads to the same results.) The grain-size data is for only one of the phases, olivine; to convert these data to equivalent roughness r, we use (A.14) with a canonical peridotite mixture (i.e., 60% olivine) to write $r = 0.5907\mathcal{R}_2$, where $\mathcal{R}_2$ is the mean olivine grain-size (see §Appendix A.2). The roughness r for the data is nondimensionalized by R for the appropriate temperatures, and thus all the dimensionless data is relative to only one dimensionless field boundary R_f given by (10).

The dimensionless roughness data is then used in (11) or (12) to estimate the stress for given free parameters $q\mathcal{D}/C$ and α (assuming $q = b = 4$, $m = n = 3$). We constrain R_m with (12a) using the grain-size, stress and temperature data for the large-grain porphyroclasts (see Table B.1), assuming the paleopiezometer is reliable at largest grain-sizes. For simplicity, we use this inferred R_m for the other samples in that field area; this assumes it is independent of temperature (i.e., the temperature dependence of R_m is dictated by that of the field boundary), which may or may not be true; indeed if R_m decreases with decreasing temperature, as suggested by the grain-boundary sliding model of Hansen et al. (2011), then the *mylonite* branches for the colder temperatures would be shifted toward even smaller grain sizes.

The damage:healing ratio $q\mathcal{D}/C$ depends on temperature as determined by rheological, grain-growth and damage partitioning fraction coefficients (see Hirth and Kohlstedt, 2003; Rozel et al., 2011; Bercovici and Ricard, 2012, 2013, 2014). The main variability in this ratio is the damage partitioning fraction f, which has some estimates for olivine (Austin and Evans, 2007; Rozel et al., 2011) but is less constrained for a polycrystalline medium. We adopt the temperature dependent relation $f(T) = f_0 \exp(-2(T/1000)^{2.9})$ inferred by Rozel et al. (2011, Fig. 5) but allow the reference value f_0 to vary toward conservative values. In particular in the main text we consider a moderate value of f_0 such that $f(1000\mathrm{K}) = 10^{-3}$ (Figure 5). Thus, since the sets of grain-size data in each field area have different temperatures, they reside on unique curves with different $q\mathcal{D}/C$.

Table B.1: Mylonite zones field data.

Ivrea zone (Jin, 1995; Jin et al., 1998)			
lithology	grain-size (μm)	temperature (°C)	stress (MPa)
porphyroclasts	2000[a]	1200	4
mylonites, protomylonites	30-80[a]	1200	?
ultramylonites	5-10[a]	800	?
Oman ophiolite (Linckens et al., 2011)			
lithology	grain-size (μm)	temperature (°C)	stress (MPa)
porphyroclasts	1500-3000[b]	1100	7
mylonites, protomylonites	300-800[c]	800	?
ultramylonites	9-43[d]	700	?

[a] Jin (1995) Table 5, samples BM9311, BM911s, BM9318ps; [b] Linckens et al. (2011) Fig 4a & Fig 9; [c] *ibid* para. 24 & Fig 9; [d] *ibid* Figs. 9 & 10

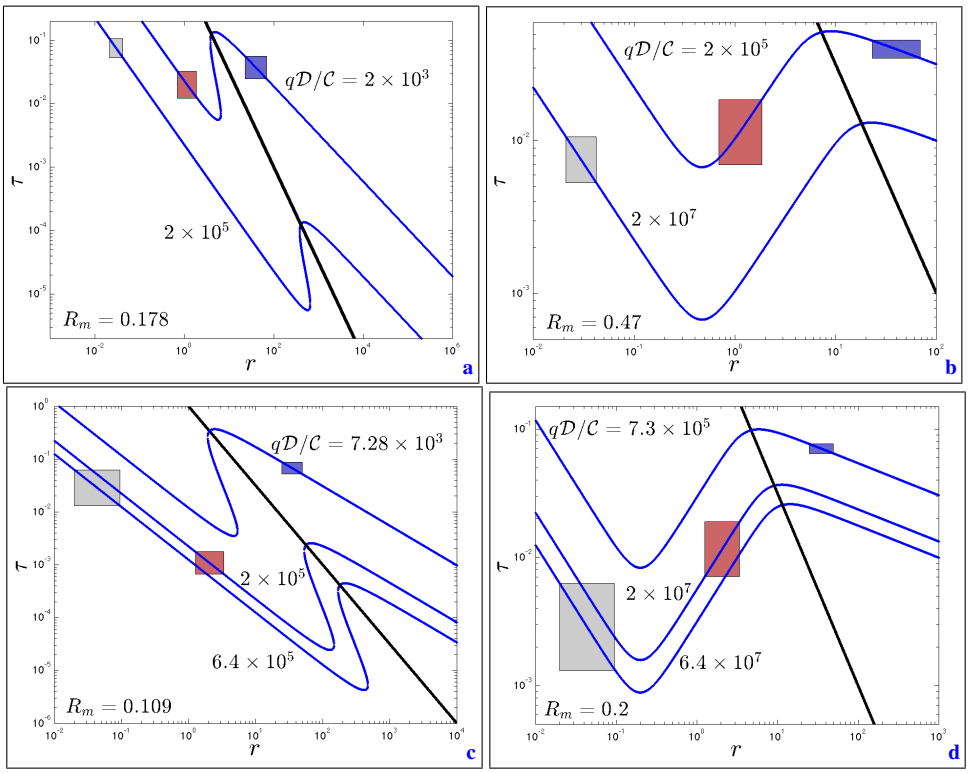

Figure B.1: Additional sample applications of the theoretical deformation maps to data from (Jin, 1995; Jin et al., 1998) (a,b) and (Linckens et al., 2011) (c,d), as summarized in Table B.1. The first column (a,c) are for $\alpha = 8/3$ and for low damage partitioning f in which $f(1000\text{K}) = 10^{-5}$. The second column (b,d) is for $\alpha = 0$ and the same $f(T)$ as in Fig 5. See Fig 5, §3.4, and Appendix B for further details.

For the sake of completeness, we also compare our theoretical deformation maps to the field data for two more cases, one involving even smaller damage, with f_0 a factor of 100 times smaller than shown in Figure 5 but the same $\alpha = 8/3$; and a case for when R_m is constant, i.e, $\alpha = 0$, but using the same f_0 as in the main text (Figure B.1). For the low damage case, all the mylonite grain-sizes fall on the *mylonite* branch, but the stress drop from the clasts' stresses is much less than for the moderate damage case; indeed, the ultramylonites have comparable stresses to those of the large-grain clasts, showing again that mylonites need not be associated with large increases in stress. Even though the case with $\alpha = 0$ cannot match the empirical piezometric curve for the *creeping* branch, it provides an example of when the system allows velocity weakening. In this case the mylonites again reside at lower stresses than for the clasts, but the protomylonites now sit on the velocity weaken-

ing *intermediate* branch, and have higher stresses than the ultramylonites, rather than lower as with $\alpha = 8/3$. The *intermediate* branch is, however, unstable, which is consistent with the inference that protomylonites are transient; i.e., they cannot stay on the branch and must evolve to one of the two stable branches.

Acknowledgments. The authors benefited greatly from discussions with Shun Karato (who also kindly provided the data from the Balmuccia study of Jin et al. (1998)), Greg Hirth, and Phil Skemer. We are also indebted to Phil Skemer (again!), Norm Sleep, Mark Behn and an anonymous referee for thorough and helpful reviews, and finally Mark Jellinek for his thoughtful handling of this paper. This work was supported by National Science Foundation Grants EAR-1344538 and EAR-1135382.

References

Austin, N., Evans, B., 2007. Paleowattmeters: A scaling relation for dynamically recrystallized grain size. Geology 35, 343–346.

Bercovici, D., 1993. A simple model of plate generation from mantle flow. Geophys. J. Int. 114, 635–650.

Bercovici, D., 1995. A source-sink model of the generation of plate tectonics from non-newtonian mantle flow. J. Geophys. Res. 100, 2013–2030.

Bercovici, D., 2003. The generation of plate tectonics from mantle convection. Earth Planet. Sci. Lett. 205, 107–121.

Bercovici, D., Karato, S., 2003. Theoretical analysis of shear localization in the lithosphere. In: Karato, S., Wenk, H. (Eds.), Reviews in Mineralogy and Geochemistry: Plastic Deformation of Minerals and Rocks. Vol. 51. Min. Soc. Am., Washington, DC, Ch. 13, pp. 387–420.

Bercovici, D., Ricard, Y., 2005. Tectonic plate generation and two-phase damage: void growth versus grainsize reduction. J. Geophys. Res. 110, B03401, doi:10.1029/2004JB003181.

Bercovici, D., Ricard, Y., 2012. Mechanisms for the generation of plate tectonics by two-phase grain-damage and pinning. Phys. Earth Planet. Int. 202-203, 27–55.

Bercovici, D., Ricard, Y., 2013. Generation of plate tectonics with two-phase grain-damage and pinning: Source–sink model and toroidal flow. Earth and Planetary Science Letters 365 (0), 275 – 288.

Bercovici, D., Ricard, Y., 2014. Plate tectonics, damage and inheritance. Nature 508, 513–516.

Bercovici, D., Schubert, G., Ricard, Y., 2015a. Abrupt tectonics and rapid slab detachment with grain damage. Proc. National Academy Sciences 112 (5), 1287–1291.

Bercovici, D., Tackley, P. J., Ricard, Y., 2015b. The Generation of Plate Tectonics from Mantle Dynamics. In: David Bercovici (Gerald Schubert editor-in-chief) (Ed.), Treatise on Geophysics, 2nd Edition. Vol. 7. Elsevier, Ch. 7, pp. 271 – 318.

Braun, J., Chery, J., Poliakov, A., Mainprice, D., Vauchez, A., Tomassi, A., Daignieres, M., 1999. A simple parameterization of strain localization in the ductile regime due to grain size reduction: A case study for olivine. J. Geophys. Res. 104, 25167–25181.

Chen, I., Argon, A., 1979. Grain boundary and interphase boundary sliding in power law creep. Acta Metallurgica 27, 749–754.

Connerney, J. E. P., Acuña, M. H., Ness, N. F., Kletetschka, G., Mitchell, D. L., Lin, R. P., Reme, H., 2005. Tectonic implications of mars crustal magnetism. Proceedings of the National Academy of Sciences of the United States of America 102 (42), 14970–14975.
URL http://www.pnas.org/content/102/42/14970.abstract

De Bresser, J., ter Heege, J., Spiers, C., 2001. Grain size reduction by dynamic recrystallization: can it result in major rheological weakening? Intl. J. Earth Sci. 90, 28–45.

Dijkstra, A. H., Drury, M. R., Vissers, R. L. M., Newman, J., Van Roermund, H. L. M., 2004. Shear zones in the upper mantle: evidence from alpine- and ophiolite-type peridotite massifs. Geological Society, London, Special Publications 224 (1), 11–24.
URL http://sp.lyellcollection.org/content/224/1/11.abstract

Dimanov, A., Rybacki, E., Wirth, R., Dresen, G., 2007. Creep and strain-dependent microstructures of synthetic anorthite–diopside aggregates. Journal of Structural Geology 29 (6), 1049 – 1069.
URL http://www.sciencedirect.com/science/article/pii/S0191814107000338

Foley, B. J., Bercovici, D., Landuyt, W., 2012. The conditions for plate tectonics on super-earths: Inferences from convection models with damage. Earth and Planetary Science Letters 331-332, 281–290.

Forsyth, D., Uyeda, S., 1975. On the relative importance of the driving forces of plate motion. Geophys. J. R. Astr. Soc. 43, 163–200.

Furusho, M., Kanagawa, K., 1999. Reaction induced strain localization in a lherzolite mylonite from the hidaka metamorphic belt of central hokkaido, japan. Tectonophysics 313, 411–432.

Gueydan, F., Précigout, J., Montési, L. G., 2014. Strain weakening enables continental plate tectonics. Tectonophysics 631 (0), 189 – 196, observational and Modelling perspectives on the Mechanical properties of the Lithosphere.
URL http://www.sciencedirect.com/science/article/pii/S0040195114000924

Gurnis, M., Hall, C., Lavier, L., 2004. Evolving force balance during incipient subduction. Geochemistry, Geophysics, Geosystems 5 (7).

Gurnis, M., Zhong, S., Toth, J., 2000. On the competing roles of fault reactivation and brittle failure in generating plate tectonics from mantle convection. In: Richards, M. A., Gordon, R., van der Hilst, R. (Eds.), History and Dynamics of Global Plate Motions, Geophys. Monogr. Ser. Vol. 121. Am. Geophys. Union, Washington, DC, pp. 73–94.

Hager, B., O'Connell, R., 1981. A simple global model of plate dynamics and mantle convection. J. Geophys. Res. 86, 4843–4867.

Hall, C., Parmentier, E. M., 2003. The influence of grain size evolution on convective instability. G^3, 1029, doi:10.1029/2002GC000308.

Hansen, L. N., Zimmerman, M. E., Kohlstedt, D. L., 2011. Grain boundary sliding in san carlos olivine: Flow law parameters and crystallographic-preferred orientation. Journal of Geophysical Research: Solid Earth 116 (B8), doi:10.1029/2011JB008220, b08201.
URL http://dx.doi.org/10.1029/2011JB008220

Herwegh, M., Linckens, J., Ebert, A., Berger, A., Brodhag, S., 2011. The role of second phases for controlling microstructural evolution in polymineralic rocks: A review. Journal of Structural Geology 33 (12), 1728 – 1750.

Hiraga, T., Tachibana, C., Ohashi, N., Sano, S., 2010. Grain growth systematics for forsterite ± enstatite aggregates: Effect of lithology on grain size in the upper mantle. Earth Planet. Sci. Lett. 291, 10–20.

Hirth, G., Kohlstedt, D., 2003. Rheology of the upper mantle and

the mantle wedge: a view from the experimentalists. In: Eiler, J. (Ed.), Subduction Factor Mongraph. Vol. 138. Am. Geophys. Union, Washington, DC, pp. 83–105.

Jin, D., 1995. Deformation microstructures of some ultramafic rocks. Master's thesis, University of Minnesota.

Jin, D., Karato, S., Obata, M., 1998. Mechanisms of shear localization in the continental lithosphere: Inference from the deformation microstructures of peridotites from the ivrea zone, northwestern italy. J. Struct. Geol. 20, 195–209.

Karato, S., 1989. Grain growth kinetics in olivine aggregates. Tectonophysics 168, 255–273.

Karato, S., 2008. Deformation of Earth Materials: An Introduction to the Rheology of Solid Earth. Cambridge Univ. Press.

Karato, S., Toriumi, M., Fujii, T., 1980. Dynamic recrystallization of olivine single crystals during high temperature creep. Geophys. Res. Lett. 7, 649–652.

Landuyt, W., Bercovici, D., 2009a. Formation and structure of lithospheric shear zones with damage. Phys. Earth Planet. Int. 175, 115–126.

Landuyt, W., Bercovici, D., 2009b. Variations in planetary convection via the effect of climate on damage. Earth Planet. Sci. Lett. 277, 29–37.

Lebrun, J.-F., Lamarche, G., Collot, J.-Y., 2003. Subduction initiation at a strike-slip plate boundary: The cenozoic pacific-australian plate boundary, south of new zealand. J. Geophys. Res. 108, doi: 10.1029/2002JB002041.

Lenardic, A., Crowley, J. W., 2012. On the notion of well-defined tectonic regimes for terrestrial planets in this solar system and others. The Astrophysical Journal 755 (2), 132.
URL http://stacks.iop.org/0004-637X/755/i=2/a=132

Lenardic, A., Jellinek, M., Moresi, L.-N., 2008. A climate change induced transition in the tectonic style of a terrestrial planet. Earth Planet. Sci. Lett. 271, 34–42.

Linckens, J., Bruijn, R. H., Skemer, P., 2014. Dynamic recrystallization and phase mixing in experimentally deformed peridotite. Earth and Planetary Science Letters 388, 134 – 142.

Linckens, J., Herwegh, M., Müntener, O., 3 2015. Small quantity but large effect —how minor phases control strain localization in upper mantle shear zones. Tectonophysics 643 (0), 26–43.

Linckens, J., Herwegh, M., Müntener, O., Mercolli, I., 2011. Evolution of a polymineralic mantle shear zone and the role of second phases in the localization of deformation. J. Geophys. Res. 116, B06210, 21 pp.

Manohar, P., Ferry, M., Chandra, T., 1998. Five decades of the zener equation. ISIJ Int. 38 (9), 913–924.

Montési, L., Hirth, G., 2003. Grain size evolution and the rheology of ductile shear zones: From laboratory experiments to postseismic creep. Earth Planet. Sci. Lett. 211, 97–110.

Ricard, Y., Bercovici, D., 2009. A continuum theory of grain size evolution and damage. J. Geophys. Res. 114, B01204, doi:10.1029/2007JB005491.

Rozel, A., Ricard, Y., Bercovici, D., 2011. A thermodynamically self-consistent damage equation for grain size evolution during dynamic recrystallization. Geophys. J. Int. 184 (2), 719–728.

Skemer, P., Warren, J. M., Kelemen, P. B., Hirth, G., 2010. Microstructural and rheological evolution of a mantle shear zone. J. Petrol. 51, 43–53.

Sleep, N., 2000. Evolution of the mode of convection within terrestrial planets. J. Geophys. Res. 105, 17,563–17,578.

Sleep, N., 2015. Evolution of the earth: Plate tectonics through time. In: D. Stevenson (G. Schubert, chief editor) (Ed.), Treatise on Geophysics, 2nd Edition. Vol. 9. Elsevier, Oxford, Ch. 6, pp. 145 – 172.
URL http://www.sciencedirect.com/science/article/pii/B9780444538024001585

Smith, C. S., 1948. Grains, phases, and interfaces: An interpretation of microstructure. Trans. A.I.M.E. 175, 15–51.

Stipp, M., Tullis, J., Scherwath, M., Berhman, J., 2010. A new perspective on paleopiezometry: Dynamically recrystallized grain size distributions indicate mechanism changes,. Geology 38 (8), 759–762.

Tackley, P., 1998. Self-consistent generation of tectonic plates in three-dimensional mantle convection. Earth Planet. Sci. Lett. 157, 9–22.

Tackley, P., 2000. Self-consistent generation of tectonic plates in time-dependent, three-dimensional mantle convection simulations, 2. strain weakening and asthenosphere. Geochem. Geophys. Geosystems (G^3) 1, 2000GC000043.

Tasaka, M., Hiraga, T., Michibayashi, K., 2014. Influence of mineral fraction on the rheological properties of forsterite+enstatite during grain size sensitive creep: 3. application of grain growth and flow laws on peridotite ultramylonite. Journal of Geophysical Research: Solid Earth 119 (2), 840–857.
URL http://dx.doi.org/10.1002/2013JB010619

Turcotte, D., Morein, G., Roberts, D., Malamud, B., 1999. Catastrophic resurfacing and episodic subduction on venus. Icarus 139 (1), 49 – 54.
URL http://www.sciencedirect.com/science/article/pii/S0019103599960840

Van der Wal, D., Chopra, P., Drury, M., FitzGerald, J., 1993. Relationships between dynamically recrystallized grain size and deformation conditions in experimentally deformed olivine rocks. Geophysical Research Letters 20 (14), 1479–1482.
URL http://dx.doi.org/10.1029/93GL01382

Warren, J. M., Hirth, G., 2006. Grain size sensitive deformation mechanisms in naturally deformed peridotites. Earth Planet. Sci. Lett. 248 (1-2), 438–450.

Weller, M., Lenardic, A., O'Neill, C., 2015. The effects of internal heating and large scale climate variations on tectonic bi-stability in terrestrial planets. Earth and Planetary Science Letters 420 (0), 85 – 94.
URL http://www.sciencedirect.com/science/article/pii/S0012821X15001648

Weller, M. B., Lenardic, A., 2012. Hysteresis in mantle convection: Plate tectonics systems. Geophysical Research Letters 39 (10), n/a–n/a.
URL http://dx.doi.org/10.1029/2012GL051232

White, S., Burrows, S., Carreras, J., Shaw, N., Humphreys, F., 1980. On mylonites in ductile shear zones. J. Struct. Geol. 2, 175–187.

Whitehead, J., Gans, R., 1974. A new, theoretically tractable earthquake model. Geophys. J. R. Astron. Soc. 39, 11–28.